Monthly Notices of the ROYAL ASTRONOMICAL SOCIETY

MNRAS **537,** 788–808 (2025) https://doi.org/10.1093/mnras/staf030
Advance Access publication 2025 January 9

Mapping dusty galaxy growth at $z > 5$ with FRESCO: detection of Hα in submm galaxy HDF850.1 and the surrounding overdense structures

Thomas Herard-Demanche [1]★ Rychard J. Bouwens,[1] Pascal A. Oesch [2,3] Rohan P. Naidu,[4] Roberto Decarli [5] Erica J. Nelson,[6] Gabriel Brammer,[2] Andrea Weibel [3] Mengyuan Xiao,[3] Mauro Stefanon,[7,8] Fabian Walter,[9] Jorryt Matthee [10] Romain A. Meyer [3,9] Stijn Wuyts [11] Naveen Reddy,[12] Lucie Rowland [1] Ivana van Leeuwen [1] Pablo Arrabal Haro [13] Helmut Dannerbauer,[14,15] Alice E. Shapley,[16] John Chisholm [17] Pieter van Dokkum,[18] Ivo Labbe,[19] Garth Illingworth,[20] Daniel Schaerer[3] and Irene Shivaei [21]

Affiliations are listed at the end of the paper

Accepted 2024 December 19. Received 2024 December 19; in original form 2023 August 24

ABSTRACT

We report the detection of a 13σ Hα emission line from HDF850.1 at $z = 5.188 \pm 0.001$ using the FRESCO (First Reionization Era Spectroscopically Complete Observations) NIRCam *F444W* grism observations. Detection of Hα in HDF850.1 is noteworthy, given its high far-infrared (IR) luminosity, substantial dust obscuration, and the historical challenges in deriving its redshift. HDF850.1 shows a clear detection in the *F444W* imaging data, distributed between a northern and southern component, mirroring that seen in [C II] from the Plateau de Bure Interferometer. Modelling the spectral energy distribution of each component separately, we find that the northern component has a higher mass, star formation rate (SFR), and dust extinction than the southern component. The observed Hα emission appears to arise entirely from the less-obscured southern component and shows a similar $\Delta v \sim +130$ km s^{-1} velocity offset to that seen for [C II] relative to the source systemic redshift. Leveraging Hα-derived redshifts from FRESCO observations, we find that HDF850.1 is forming in one of the richest environments identified to date at $z > 5$, with 100 $z = 5.17$–5.20 galaxies distributed across 13 smaller structures and a $\sim$(15 cMpc)^3 volume. Based on the evolution of analogous structures in cosmological simulations, the $z = 5.17$–5.20 structures seem likely to collapse into a single $> 10^{14}$M$_\odot$ cluster by $z \sim 0$. Comparing galaxy properties forming within this overdensity with those outside, we find the masses, SFRs, and *UV* luminosities inside the overdensity to be clearly higher. The prominence of Hα line emission from HDF850.1 and other known highly obscured $z > 5$ galaxies illustrates the potential of NIRCam-grism programs to map both the early build-up of IR-luminous galaxies and overdense structures.

Key words: galaxies: evolution – galaxies: high-redshift – large-scale structure of Universe – submillimetre: galaxies.

1 INTRODUCTION

One of the most important frontiers in extragalactic astronomy has been understanding the formation and evolution of massive galaxies in the early universe. Despite the many significant insights that have been gained into both the build-up of the star formation rates (SFRs) and stellar masses of *UV*-bright galaxies from both space and ground-based telescopes (e.g. Madau & Dickinson 2014; Davidzon et al. 2017; Bouwens et al. 2021; Stefanon et al. 2021; Harikane et al. 2022), it is essential we achieve an equally complete census of star formation from obscured galaxies given how significantly obscured star formation contributes to galaxies with masses $> 10^{10}$M$_\odot$ (e.g. Reddy et al. 2006, 2008; Whitaker et al. 2017).

In addition to the great strides made by the Atacama Large Millimeter/submillimeter Array (ALMA) in this area (e.g. Casey et al. 2021; Smail et al. 2021; Bouwens et al. 2022; Dayal et al. 2022), *JWST* is further revolutionizing this science area thanks to its sensitive near-infrared (IR) photometric and spectroscopic capabilities to 5μm and beyond, sampling bright Balmer lines like Hα to $z \sim 7$ (e.g. Helton et al. 2024; Oesch et al. 2023) and Paschen series line like Paα and Paβ mostly at intermediate redshifts (e.g. Reddy et al. 2023) and in at least one case at $z \sim 7$ (Álvarez-Márquez et al. 2023). Through the identification of bright line emission from e.g. Hα (e.g. the candidate $z = 5.58$ dusty galaxy shown in Oesch et al. 2023), one can assemble substantial spectroscopic samples of far-IR luminous, dusty star-forming galaxies in the early universe with *JWST*. Particularly useful for this endeavor are NIRCam grism observations that allow for a probe of Hα emission over the full morphology of sources over a $\sim$9 arcmin^2 NIRCam field, facilitating redshift determinations even when the escape of Hα occurs over just an isolated region.

In this paper, we report on the successful detection of Hα emission from HDF850.1, one of the first submillimetre galaxies

★ E-mail: herard@strw.leidenuniv.nl

to be identified in the high-redshift universe, leveraging new grism observations from the First Reionization Era Spectroscopically Complete Observations (FRESCO: Oesch et al. 2023) program. HDF850.1 was initially identified using sensitive submillimetre observations over the Hubble Deep Field (HDF) North with the SCUBA (Submillimetre Common-User Bolometer Array STScI) camera (Hughes et al. 1998), but no optical counterpart could be identified in the deepest *Hubble Space Telescope* (*HST*) images available at the time. Based on the available information, HDF 850.1 appeared to have a redshift $z > 2$, implying that the SFR of this single source could rival the total star formation activity of all coeval galaxies in the HDF combined. This discovery triggered a >10-yr effort to improve the location of the source from the coarse position provided by the 17 arcsec full width at half-maximum (FWHM) SCUBA beam, to search for possible counterparts, and to pin down its redshift (Downes et al. 1999; Richards 1999; Dunlop et al. 2004; Wagg et al. 2007; Cowie et al. 2009).

A redshift for HDF 850.1 was finally obtained through a millimetre line scan obtained at the Institut de radioastronomie millimétrique (IRAM) Plateau de Bure Interferometer (PdBI) by Walter et al. (2012) who detected multiple lines in the rest-frame submillimetre ([C II] as well as multiple CO lines), thus unambigously pinpointing the redshift to $z = 5.183$. This study also revealed that the system is part of a fairly significant galaxy overdensity at these redshifts. Higher resolution imaging of the [C II] line emission from HDF 850.1 (Neri et al. 2014) provided evidence that HDF 850.1 is a merging system.

In addition to enabling the detection of the Hα line from HDF850.1, the new NIRCam imaging observations from FRESCO allow us to measure the continuum flux from HDF850.1 in the rest-optical while facilitating a modelling of the overall spectral energy distribution (SED) of both components of the source. Moreover, the NIRCam grism observations allow for the identification of a large number of Hα emitters over a ∼62 arcmin^2 FRESCO area in the GOODS North field, allowing us to map out the $z = 5.17$–5.20 overdensity much more extensively than had been possible in earlier work by Walter et al. (2012), Arrabal Haro et al. (2018), and Calvi et al. (2021).

We organize the paper as follows. In Section 2, we provide a summary of the observational data we utilize for this analysis and describe our procedures for constructing multiwavelength catalogues. In Section 3, we describe our discovery of a detection of Hα from HDF850.1, the photometry we derive for the two components of HDF850.1 and inferences based on SED modelling, and then present information on both the structure of the $z = 5.17$–5.20 overdensity in which HDF850.1 resides, and on the characteristics of the large number of other member galaxies. In Section 4, we include a short summary of our primary results and provide a brief look to the future. For consistency with previous work, we express all quantities using the so-called concordance cosmology with $\Omega_m = 0.3$, $\Omega_\Lambda = 0.7$, and $H_0 = 70 \mathrm{km\,s^{-1}\,Mpc^{-1}}$. Stellar masses and SFRs are presented assuming a Chabrier (2003) initial mass function (IMF). All magnitudes are presented using the AB magnitude system (Oke & Gunn 1983).

2 DATA

2.1 FRESCO NIRCam grism and imaging data

In this analysis, we make use of NIRCam data obtained by the *JWST* FRESCO survey (GO-1895; see Oesch et al. 2023 for details). FRESCO covered both the GOODS-South and the GOODS-North fields with ∼62 arcmin^2 of NIRCam/grism spectroscopy in the *F*444*W* filter. This coverage is achieved with two 2×4 mosaics of NIRCam/grism observations with significant column overlap in order to maximize the wavelength coverage over the field. Only the GRISMR was used due to overhead costs. The maximal wavelength coverage is from 3.8 to 5.0 μm, which is achieved over 73 per cent of the full mosaic. The exposure times per pointing are 7043 s, resulting in an average 5σ line sensitivity of $\sim 2 \times 10^{-18}$ erg s^{-1} cm^{-2} at a resolution of $R \sim 1600$. The grism data of GOODS-N used here were obtained in 2023 February.

The NIRCam/grism observations are reduced using the publicly available GRIZLI code[1] (see also Brammer et al., in preparation). Specifically, we start from the rate files that are obtained from the Mikulski Archive for Space Telescopes archive. These are then aligned to a *Gaia*-matched reference frame. The direct images of a given visit are used to align the associated grism exposures. Before combination of the long-wavelength data, a custom bad-pixel map is applied, which masks residual bad pixels.

Following Kashino et al. (2023), we use a median filtering technique to remove the continuum spectra for each row of the individual grism exposures. The filter uses a 12 pixel central gap, which avoids self-subtraction in case of strong emission lines. After the first pass filtering, pixels with significant line flux are identified and masked, before running the median filtering again.

For each source of interest from the photometric catalogue (see the next section), we derive an extraction kernel based on the image morphology in the *F*444*W* band and the segmentation map. This kernel is used to perform an optimal extraction of 1D spectra from the aligned and combined grism exposures. We use slightly modified sensitivity curves and spectral traces based on the v4 grism configuration files.[2]

In addition to the grism observations, FRESCO obtained imaging in the two short-wavelength filters *F*182*M* and *F*210*M*, as well as direct imaging in the long-wavelength filter *F*444*W*. The 5σ depths of these images are, respectively, 28.3, 28.1, and 28.2 mag, as measured in circular apertures of 0.32 arcsec diameter.

We note that deeper NIRCam imaging data are available over ∼50 per cent of the FRESCO mosaics thanks to observations from the JWST Advanced Deep Extragalactic Survey (JADES) team (Robertson 2022). However, these data are not yet publicly available for inclusion in this analysis.

2.2 FRESCO multiwavelength catalogues

In addition to the new *JWST* NIRCam data, we also make use of all ancillary *HST* imaging available in the GOODS-North field. Being a key extragalactic field for more than a decade, GOODS North has been targeted by all the main telescope facilities through a large number of programs. A complete listing of *HST* programs can be found on the Hubble Legacy Field (HLF) release page[3] (see also Illingworth et al. 2016; Whitaker et al. 2019). Most importantly, the field was covered with ACS imaging from GOODS (Giavalisco et al. 2004), with ACS and WFC3/IR imaging by the CANDELS survey (Grogin et al. 2011; Koekemoer et al. 2011), as well as WFC3/IR grism imaging by the AGHAST survey (Weiner & AGHAST Team 2014).

Here, we use a re-reduction of all available *HST* ACS and WFC3/IR data in the archive in filters that cover the FRESCO pointings, which we drizzled to a common pixel frame of 40 mas pixel^{-1}

[1] https://github.com/gbrammer/grizli
[2] https://github.com/npirzkal/GRISMCONF
[3] https://archive.stsci.edu/prepds/hlf/

as the *JWST* NIRCam data. The 5σ depth (in the same 0.32 arcsec diameter apertures) for the ancillary data are well matched to the FRESCO NIRCam imaging: they range from ∼28.6 mag for the ACS data (*F*435*W*, *F*606*W*, *F*775*W*, *F*814*W*, and *F*850*LP*) to ∼28.2 mag for the WFC3/IR data (*F*105*W*, *F*125*W*, and *F*160*W*), with the exception of *F*140*W* that reaches to ∼ 27.4 mag.

In total, we derive photometry in 12 bands for the GOODS-North data set. The *F*444*W* images are used as a detection image, and we run SExtractor (Bertin & Arnouts 1996) in dual-image mode to measure matched-aperture photometry. The images are all point spread function (PSF) matched to the *F*444*W* detection image, and fluxes are corrected to total using the default SExtractorAUTO parameters in addition to a small correction for remaining flux outside the AUTO aperture based on WebbPSF's *F*444*W* curve of growth (Perrin et al. 2014).

2.3 Spectroscopic sample of Hα emitters

We briefly summarize the construction of the Hα catalogue at $z \approx 4.9 - 6.6$ over the GOODS-North FRESCO field and refer readers to Brammer et al. (in preparation) and Naidu et al. (in preparation) for more detailed description of the overall methods and catalogue validation. Line extractions from the grism data are based on EAZY photometric redshifts ($z_{\rm phot}$). For each object, we search for lines in a window around $z_{\rm phot} \pm 0.05 \times (1 + z_{\rm phot})$, corresponding to the mean 1σ width of the redshift-likelihood distribution function of all Hα emitters in our sample (after 3σ clipping). The photometric redshifts are derived from the PSF-matched photometry described above (Section 2.2). Additionally, we also use the default GRIZLI photometric redshifts catalogue that uses a stack of the FRESCO imaging (*F*182*M* + *F*210*M* + *F*444*W*) as a detection image, and makes two different choices in performing the photometry (e.g. with different source deblending parameters). We use both sets of photometric redshifts to marginalize over such choices. In practice, the best-fitting redshifts at $z_{\rm phot} > 4.5$ have a small median difference of $|\Delta_z| < 0.1$ and in most cases result in the same line candidates, but a fraction (≈ 25 per cent) have $|\Delta_z| > 0.3$.

Every line extracted with S/N > 5 is visually inspected to verify that its morphology is consistent with the source and also to look for false positives (e.g. from broad polycyclic aromatic hydrocarbon features in the foreground that slip through the median filtering). Physical properties (e.g. stellar masses) are derived by jointly fitting the photometry and line fluxes with a non-parametric star formation history (SFH) and Chabrier IMF using the PROSPECTOR SED-fitting code (Leja et al. 2017). We refer readers to Naidu et al. (in preparation) for further details about the modelling choices. To assess the robustness of Hα-emitters identified as part of our selection, we compare our catalogue to those from the independent analyses made in Sun et al. (2024) and also Covelo-Paz et al. (2024). Over the same redshift range as considered here and only considering detections with $\mathrm{SNR}_{\mathrm{H}_\alpha} > 5$, Sun et al. (2024) find 100 sources where we find 75, conducting a search over those areas of FRESCO that overlap with the JADES photometric data set in GOODS North. Those numbers include six multicomponent sources whose clumps are counted as different sources in one of the two catalogues. We investigated the 25 Hα emitters from the Sun et al. (2024) catalogue not found in our own catalogues. Among these 25, 14 are in the general FRESCO catalogue but were either associated with different lines than Hα (three sources) or which were flagged due to heavily contaminated spectra from other nearby galaxies (11 sources). As such, we can conclude that most of the differences that occur between our catalogues result from the differing robustness criteria we apply. Comparing our Hα selection with Covelo-Paz et al. (2024), we find ∼93 per cent overlap with their selection, providing further evidence for the reliability of our Hα catalogue.

Regarding completeness, we assume the results of Covelo-Paz et al. (2024) largely apply to our own selection given the >90 per cent overlap between our catalogues and similar line identification procedures. Covelo-Paz et al. (2024) estimate the total completeness for their selection by multiplying together the completeness function determined from four separate steps (1) photometric detection, (2) extraction, (3) line detection, and (4) visual inspection (see section 3 of Covelo-Paz et al. 2024 for details). The completeness of Hα-emitter selections over FRESCO is >70 per cent complete for Hα fluxes in excess of 3×10^{-18}erg s^{-1} cm^{-2} and detection magnitudes of < 27 mag. As 60 per cent of our catalogue satisfy both of those conditions, our catalogue should include the majority (>70 per cent) of Hα emitting galaxies to 27 mag.

3 RESULTS

3.1 Identification of Hα emission from HDF850.1

One of the first sources we examined after creating catalogues of line emitting sources over the GOODS-North FRESCO field was the well-known dusty star-forming galaxy HDF850.1 with a spectroscopic redshift $z = 5.1853$ from the 157.74 μm [C II] line (Walter et al. 2012; Neri et al. 2014). As we discussed in Introduction, that source evaded a direct redshift determination for >10 yr following its initial discovery (e.g. Wagg et al. 2007), and a redshift only came in 2012 thanks to a dedicated spectral scan for [C II] and various CO lines with PdBI (Walter et al. 2012).

The *JWST* *F*182*M*, *F*210*M*, and *F*444*W* NIRCam imaging we have available for HDF850.1 from FRESCO is shown in the centre and right panels of Fig. 1 together with the blueshifted and redshifted high spatial resolution [C II] contours from PdBI. Also shown is the imaging data of HDF850.1 at 0.8 μm from *F*814*W*, again demonstrating that HDF850.1 radiates essentially no flux at < 1μm. From this imaging data, it is clear that while both components are detected in the NIRCam *F*444*W* data, only the southern component shows a clear detection in the *F*182*M* and *F*210*M* imaging data.

We made use of the two prominent components of HDF850.1 in the *F*444*W* imaging data to construct segmentation maps, shown in the central and right panels of Fig. 1 as red and blue dashed lines. We then used GRIZLI to extract spectra of each component. In Fig. 2, we show both a 2D and 1D spectral extraction for the southern component to HDF850.1. In the lower panel to Fig. 2, we present a collapsed 1D spectrum which not only reveals a 13σ detection of the Hα line, but shows the detection of $[\mathrm{N\,II}]_{6583}$ at 4σ from HDF850.1. No significant detection of $[\mathrm{N\,II}]_{6548}$ is apparent in the FRESCO grism spectra, but this is not surprising given the fact that $[\mathrm{N\,II}]_{6548}$ is ≈ 3× fainter than $[\mathrm{N\,II}]_{6583}$ (e.g. Dojčinović, Kovačević-Dojčinović & Popović 2023).

For Hα, we measure a total flux of $(6.4 \pm 0.5) \times 10^{-18}$erg s^{-1} cm^{-2} for the southern component to HDF850.1 and derive a redshift of 5.188±0.001. The $[\mathrm{N\,II}]$/Hα ratio we measure for the southern component to HDF850.1 is 0.4 ± 0.1. Such a high $[\mathrm{N\,II}]$/Hα ratio is commonly found for galaxies at higher masses with solar metallicities (e.g. Shapley et al. 2015). Shocks could also be a contributing factor to the high $[\mathrm{N\,II}]$/Hα ratio we find (e.g. Kewley et al. 2013; Freeman et al. 2019) – which would not be especially surprising given the apparent merging activity in HDF850.1 based on its two component structure (Neri et al. 2014).

The redshift measurement we derived from the Hα line implies a velocity offset of 133±34 km s^{-1} relative the systemic redshift

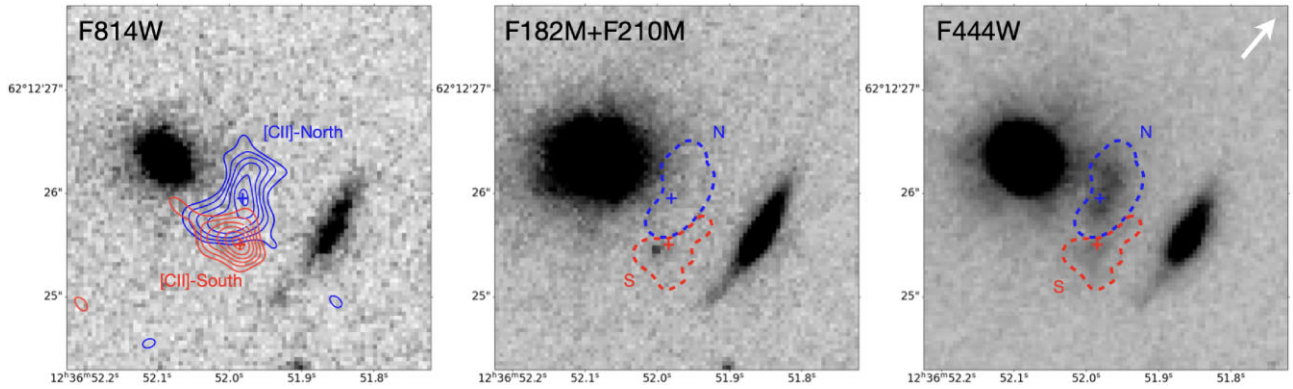

Figure 1. Images centred on HDF850.1 from both *HST* in the *F*814*W* band (left panel) and *JWST*/NIRCam in the *F*182*M* + *F*210*M* (centre panel), and *F*444*W* bands (right panel). The blue and red solid lines contours in the left panel show the 3σ, 4σ, 5σ, 6σ, 7σ, and 8σ contours for [C II] emission from the northern and southern components, respectively, of HDF850.1 as derived by Neri et al. (2014) using PdBI. Crosses give the spatial position where the [C II] emission for each component reaches a peak. The dashed contours shown in the centre and right panels delineate the regions used in our extractions of near-IR spectra for the northern (blue) and southern (red) components. These two regions have been designed to mirror the shape and morphology of the two components in the *F*444*W* imaging data. The white arrow in the upper right corner of the right panel shows the dispersion direction of the NIRCam grism.

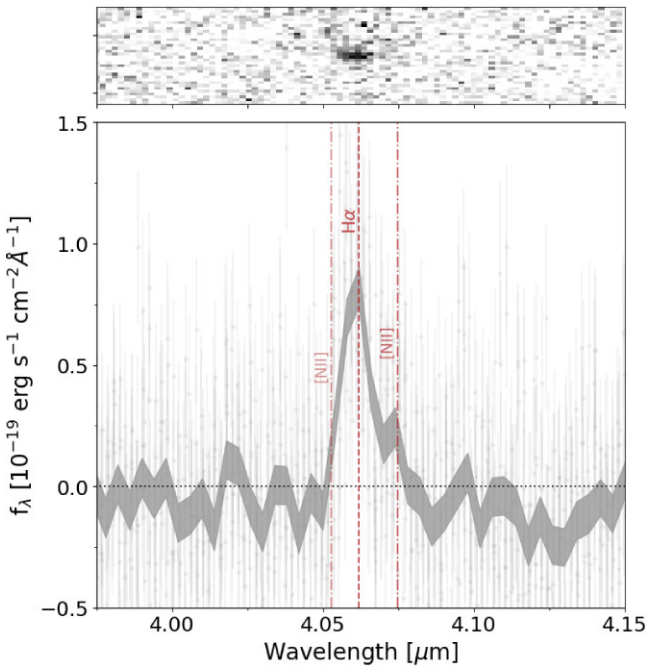

Figure 2. 2D spectrum from the southern component to HDF850.1 (upper panel) along with our 1D extraction from the direct image morphology (lower panel). The upper panel shows a zoomed-in 2D spectrum around the Hα line after subtracting the continuum using a median-filtered technique following (Kashino et al. 2023: see Section 2.1). The lower panel shows the 1D spectrum shaded in dark grey along with the collapsed 2D spectrum presented above. The dashed vertical lines show the positions of the Hα line (13σ detection) and the [N II]$_{6585}$ line (4σ detection) at the fitted redshift of $z = 5.188$. The expected wavelength of the [N II]$_{6549}$ line ($\approx 3\times$ fainter than [N II]$_{6585}$: e.g. Dojčinović et al. 2023) is also shown, but does not show a significant detection in the FRESCO data.

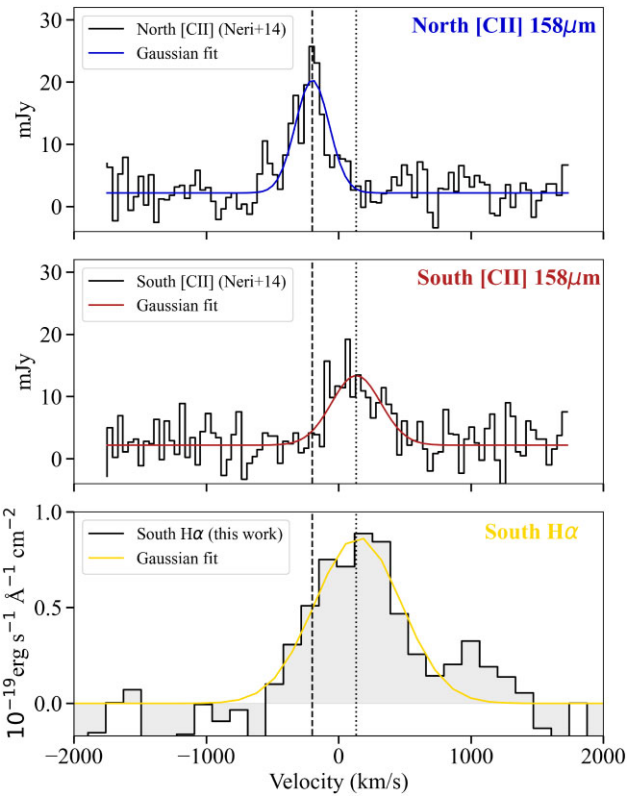

Figure 3. Comparison between the [C II] detection from Neri et al. (2014) and our Hα detection for both components. The upper two rows show the [C II] $P_{3/2} \rightarrow P_{1/2}$ line above the dust continuum from both component of HDF850.1 (black lines) as well as the Gaussian fit to the lines (blue and red lines) derived by Neri et al. (2014). The lowest row shows our detected Hα line (black) along with a Gaussian fit for the southern component (yellow). Velocities for the [C II]$_{158\mu m}$ and Hα lines are shown relative to the [C II] redshift determined by Neri et al. (2014) of $z = 5.1853$ (307.267 GHz). The dashed and dotted vertical lines are shown at the centroids of the Gaussian fits to [C II] for the northern and southern components of HDF850.1, respectively, to highlight the coinciding feature in the southern component.

measurement $z = 5.1853$ derived by Neri et al. (2014). Neri et al. (2014) find a velocity offset of 130 km s^{-1} for the [C II] line from the southern component to HDF850.1, which is almost exactly the same velocity offset in [C II] for the southern component as we find here. A detailed comparison of the line profiles and intensity of our new Hα detection is shown in Fig. 3 for the southern component to

HDF850.1, both in terms of the raw extraction (grey histogram) and Gaussian fits to the lines (yellow lines). Fig. 3 also shows the line profiles for the northern and southern components to HDF850.1 as found by Neri et al. (2014). To further emphasize this similarity, a vertical dotted line is shown at the velocity offset for the southern component found by Neri et al. (2014). From Fig. 4, it is furthermore clear that Hα emission we detect (white contours) appears to mostly originate from the southern component of HDF850.1, being offset from both the [C II] and continuum IR emission lying to the north (blue and orange contours, respectively).

Additionally, the Hα line we extract from the southern component of HDF850.1 appears to be very broad overall. Ignoring for the moment the impact spatial extension has on the width of the lines, the best-fitting FWHM we find for the southern component is of 7.6×10^2km s^{-1}. To account for the impact that source morphology has in broadening the line, we make use of GRIZLI to forward model the source based on its direct image morphology using the same dispersion direction as in the observations. Based on this forward modelling, we find that the non-zero size of HDF850.1 contributes 6.2×10^2km s^{-1} to the measured FWHMs. Subtracting this contribution in quadrature from the southern component, we derive an FWHM of $(4.4\pm0.9)\times10^2$km s^{-1}. The width of this line is therefore consistent with what Neri et al. (2014) derive for [C II] from the southern component. Given similar velocity offsets for both lines (130 km s^{-1} for [C II] versus $(1.3\pm0.3)\times10^2$km s^{-1} for Hα), it seems clear that interstellar medium (ISM) material producing both lines show a very similar kinematic structure.

In contrast to the southern component, the northern component of HDF850.1 does not show a clear, localized detection of Hα line emission. As a result and due to the proximity of the two components and dispersion direction (shown in Fig. 1), line emission from the southern component partially extends into the same spatial region where Hα line flux measurements need to be made for the northern component. As a result of these challenges, we only report an upper limit to the Hα flux for the northern component of $f_{\rm H\alpha} < 2.1\times10^{-18}$erg s^{-1} cm^{-2} ($3\sigma$). We derived this upper limit by comparing the observations with the spatial profile expected for Hα emission from the northern component assuming a similar spatial distribution to the continuum light in the direct image. By computing the 2D least-squares residuals between the expected and observed line morphologies, we concluded that there is no significant Hα line flux emanating from the northern component, and any line flux evident in the segmentation map for the northern component is consistent with contamination from the southern component. The flux measurements for the two components are provided in Table 1.

3.2 Impact of dust obscuration on the Hα line emission

Thanks to our new measurements of the Hα fluxes for both components of HDF850.1, we can compute an observed SFR for each component. By comparing this SFR to the SFR implied by the respective [C II] luminosities, we can attempt to estimate the approximate dust obscuration of each component. We use the conversion factor from Kennicutt & Evans (2012):[4]

$$\mathrm{SFR_{H\alpha}} = L_{\rm H\alpha}/(10^{41.27}\,\mathrm{erg\,s^{-1}})(\mathrm{M_\odot\,yr^{-1}}) \quad (1)$$

[4]While we present SFRs and stellar masses using the Chabrier (2003) IMF and Kennicutt & Evans (2012) present their SFR relations using Kroupa & Weidner (2003) IMF, Kennicutt & Evans (2012) emphasize that the relation for a Chabrier (2003) IMF is virtually identical.

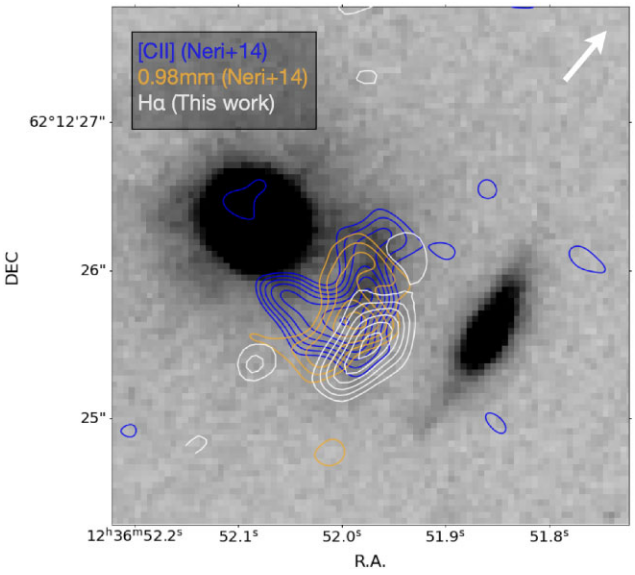

Figure 4. Spatial distribution of line and dust emission relative to the *JWST* NIRCam *F444W* imaging observations of HDF850.1. The extracted Hα map is shown in white contours over the *JWST* NIRCam *F444W* imaging. The velocity averaged [C II]$_{158\mu\rm m}$ line detection and the 0.98 mm dust continuum from Neri et al. (2014) are shown for comparison. All contours start at 3σ and increase in steps of 1σ.

The SFR we estimate from the observed Hα flux for the southern component is 6.0 ± 0.5 $(1.5/\mu)$ M$_\odot$ yr^{-1}, while for the northern component the SFR we estimate is <1.8 $(1.7/\mu)$ M$_\odot$ yr^{-1}. In specifying the SFR for each source, we have divided the result by the fiducial magnification factors for the two components derived in Neri et al. (2014) based on the isothermal model they constructed for a nearby $z = 1.224$ elliptical galaxy, i.e. 1.7 for the northern component and 1.5 for the southern component. Our quoted results in Table 1 include the factors $(1.7/\mu)$ and $(1.5/\mu)$ for clarity and to allow for a scaling of the results in case of updated lensing magnification factors.

We can estimate the approximate dust extinction for each component by relying on multiple total SFR tracers, we use the [C II] luminosities for HDF850.1 from Neri et al. (2014) as well as the inferred SFRs and IR luminosity from the BAGPIPES and MAGPHYS modelling. The ALPINE program (Béthermin et al. 2020; Faisst et al. 2020; Le Fèvre et al. 2020) provided the following calibration of the $L_{\rm [CII]}$-SFR relation (Schaerer et al. 2020):

$$\mathrm{SFR_{[CII]}} = (L_{\rm [CII]}/10^{6.61}\mathrm{L_\odot})^{0.855}(\mathrm{M_\odot\,yr^{-1}}) \quad (2)$$

We infer [C II] SFRs of $(1.6\pm0.5)\times10^2(1.7/\mu)$ M$_\odot$ yr^{-1} and $(0.9\pm0.3)\times10^2(1.5/\mu)$ M$_\odot$ yr^{-1} for the northern and southern components to HDF850.1.

Dividing the apparent Hα SFRs by the [C II] SFRs, we infer $\mathrm{SFR_{H\alpha}/SFR_{[CII]}}$ ratios of <0.01 and 0.07 ± 0.03, respectively. However, given the uncertain reliability of this tracer due to the infamous [C II] deficit (Díaz-Santos et al. 2013). We also consider the total IR luminosity following the method in Kennicutt & Evans (2012):

$$\mathrm{SFR_{TIR}} = L_{\rm TIR}/(10^{43.41}\,\mathrm{erg\,s^{-1}})(\mathrm{M_\odot\,yr^{-1}}) \quad (3)$$

If we rely on the total IR luminosities we infer for the two components from our MAGPHYS SED modelling (Section 3.3.2), we infer SFRs of $412^{+449}_{-210}(1.7/\mu)$ and $354^{+457}_{-276}(1.5/\mu)$ M$_\odot$ yr^{-1}. This leads to $\mathrm{SFR_{H\alpha}/SFR_{TIR}}$ ratios of <0.005 and $0.02^{+0.01}_{-0.02}$, respectively. Alternatively, if we rely on those from our BAGPIPES SED modelling (Section 3.3.2), we obtain $119^{+31}_{-49}(1.7/\mu)$ and $90^{+22}_{-25}(1.5/\mu)$ M$_\odot$ yr^{-1}.

Table 1. Inferred characteristics of the two components of HDF850.1.

	Northern component	
Lensing magnification μ	1.7^a	
$L_{[CII]}$	$1.6\times10^9(1.7/\mu)^a L_\odot$	
$SFR_{[CII]}$	$(1.6\pm0.5)\times10^2(1.7/\mu)^a$ $M_\odot$ yr^{-1}	
$v_{[CII]}$	-200 km s^{-1}	
$FWHM_{[CII]}$	300 km s^{-1}	
$f_{H\alpha}$	$< 2.1\times10^{-18}$erg s^{-1} cm^{-2}[3σ]	
$SFR_{H\alpha}$	$<1.8\ (1.7/\mu)M_\odot$ yr^{-1}	
$SFR_{H\alpha}/SFR_{[CII]}$	<0.01	
	MAGPHYS	BAGPIPES
A_V	$4.3^{+2.9}_{-1.8}$	$4.0^{+0.4}_{-0.3}$
$\log_{10} M_*/M_\odot$	$10.7^{+0.2}_{-0.2}+\log_{10}(1.7/\mu)$	$10.8^{+0.2}_{-0.2}+\log_{10}(1.7/\mu)$
$\log_{10} L_{IR}$	$12.4^{+0.1}_{-0.3}+\log_{10}(1.7/\mu)$	$11.9^{+0.1}_{-0.3}+\log_{10}(1.7/\mu)$
SFR	$220^{+240}_{-112}(1.7/\mu)$ $M_\odot$ yr^{-1}	$158^{+52}_{-41}(1.7/\mu)M_\odot$ yr^{-1}
	Southern component	
Lensing magnification μ	1.5^a	
$L_{[CII]}$	$0.8\times10^9(1.5/\mu)^a L_\odot$	
$SFR_{[CII]}$	$(0.9\pm0.3)\times10^2(1.5/\mu)^a$ $M_\odot$ yr^{-1}	
$v_{[CII]}$	130^akm s^{-1}	
$FWHM_{[CII]}$	410 km s^{-1}	
$f_{H\alpha}$	$(6.5\pm0.4)\times10^{-18}$erg s^{-1} cm^{-2}	
$v_{H\alpha}$	$(1.3\pm0.3)\times10^2$km s^{-1}	
$FWHM_{H\alpha+[NII]}$	$(4.4\pm0.9)\times10^2$km s^{-1}	
$SFR_{H\alpha}$	$(6.5\pm0.5)(1.5/\mu)M_\odot$ yr^{-1}	
$SFR_{H\alpha}/SFR_{[CII]}$	0.07 ± 0.03	
	MAGPHYS	BAGPIPES
A_V	$4.7^{+2.5}_{-2.0}$	$3.5^{+0.8}_{-0.4}$
$\log_{10} M_*/M_\odot$	$10.6^{+0.4}_{-0.6}+\log_{10}(1.5/\mu)$	$10.1^{+0.4}_{-0.4}+\log_{10}(1.5/\mu)$
$\log_{10} L_{IR}$	$12.4^{+0.4}_{-0.7}+\log_{10}(1.5/\mu)$	$11.7^{+0.2}_{-0.3}+\log_{10}(1.5/\mu)$
SFR	$187^{+241}_{-146}(1.5/\mu)$ $M_\odot$ yr^{-1}	$84^{+30}_{-26}(1.5/\mu)$ $M_\odot$ yr^{-1}

[a]From Neri et al. (2014).

This leads to $SFR_{H\alpha}/SFR_{TIR}$ ratios of <0.02 and 0.07 ± 0.02, respectively, for the two components. Similar SFR fractions are also obtained utilizing the SFRs we infer from BAGPIPES SED modelling (Section 3.3.2) and by making use of the inferred A_V (∼3.5–4.7 mag) from the SED modelling (Table 1).

Collectively, these results demonstrate that even with a clear detection of Hα from HDF850.1 dust attenuation has a substantial impact on the observed line emission.

3.3 UV+optical + far-IR SED model of HDF850.1

3.3.1 Photometry on the individual components of HDF850.1

Because of the very extended wings to the profile from a bright nearby elliptical galaxy, obtaining accurate flux measurements for HDF850.1 can be challenging to obtain using simple aperture photometry and therefore we elected to measure the flux for HDF850.1 by modelling the light with analytic Sérsic profiles using GALFIT (Peng et al. 2002). This provides a very effective way of coping with contamination from the bright elliptical spilling over onto our aperture measurements.

Table 2. Photometry derived for HDF850.1.

Band	Flux [AB mag][a,b]
Northern component	
F435W	>29.0
F606W	>28.9
F775W	>29.2
F850LP	>28.5
F105W	>28.5
F125W	>28.3
F140W	>27.4
F160W	>28.2
F182M	>27.4
F210M	>27.2
F444W	24.2±0.1
Southern component	
F435W	>29.0
F606W	>28.9
F775W	>29.2
F850LP	>28.5
F105W	>28.5
F125W	>28.3
F140W	>27.4
F160W	>28.2
F182M	28.0±0.3
F210M	27.8±0.3
F444W	25.7±0.3

Notes. [a] Derived using GALFIT (Peng et al. 2002: Section 3.3.1).
[b] Upper limits are 2σ.

We begin by using GALFIT to model the light in the NIRCam *F444W* band where both the northern and southern components of HDF850.1 are clearly detected, while also fitting to light in the nearby elliptical galaxy. We model the light in the southern component of HDF850.1 with a single Sérsic profile and the light from the northern component with 1, 2, and 3 profiles (fixing the centres of each component to be cospatial). To account for the uncertainties associated with the extended wings of the nearby elliptical galaxy and the star-forming arc westward to HDF850.1, we mask HDF850.1 and fit the light profile of the two prominent foreground galaxies with Sérsic profiles. We then fix the light profiles of the two foreground galaxies, unmask the HDF850.1 region, and fit the two components of HDF850.1 with Sérsic profiles. To estimate uncertainties on the flux of HDF850.1, we repeat these fits 12 ($= 2\times2\times3$) different times, alternatively modelling the flux of the foreground lensing galaxy (to the east) with one and two Sérsic cocentric profiles, the star-forming lensed arc (to the west) with one and two Sérsic profiles, the northern component with one, two, and three Sérsic profiles, and the southern component with just one Sérsic profile. We take the flux to be equal to the mean derived from these fits. For each galaxy and fit, we fix the center to that inferred from the *F444W* NIRCam imaging data.

We present the flux measurements we obtained for the two components of HDF850.1 in Table 2, the values represent the mean of the fits in each band and the errors are taken as their standard deviation. We measure an *F444W*-band magnitude of 24.2±0.1 mag for the northern component to HDF850.1 and 25.7±0.2 mag for the southern component. We remark that the *F444W* flux we measure for the southern component is ∼ 4× what we would expect accounting for the line emission from Hα alone, suggesting that

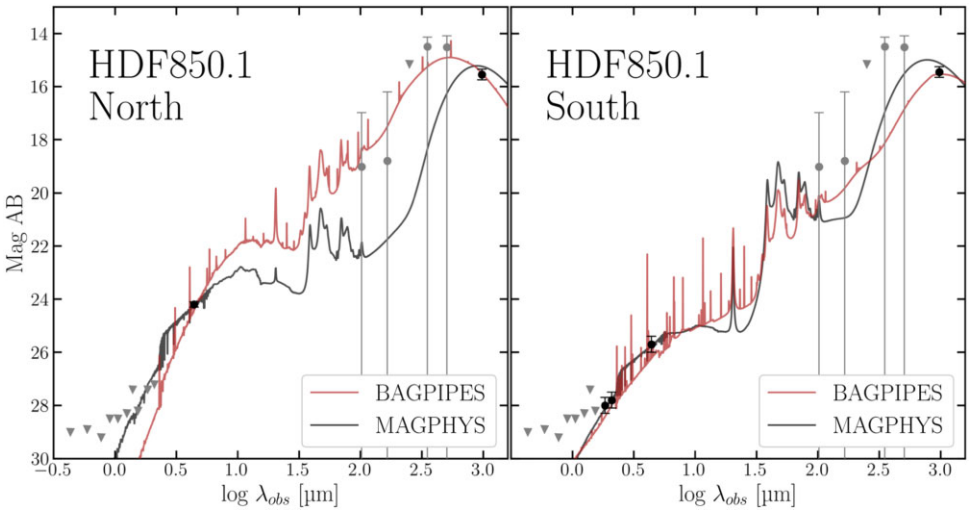

Figure 5. Model SED derived by BAGPIPES (red) and MAGPHYS (black) to the northern and southern components of HDF850.1. Optical and near-IR photometry shown with the solid circles (and 1σ uncertainties) for both components are from Table 2 and the far-IR constraints from *Herschel* as presented in Walter et al. (2012) as well as the dust continuum at 0.9 mm from Neri et al. (2014). We also take into account the *Herschel* SPIRE constraints detailed in Section 3.3.2. Upper limits on *HST* bands and *Herschel* SPIRE 250 μm are shown with grey triangles (2σ). Since the spatial resolution of the *Herschel* observations (>15 arcsec) is insufficient to provide independent measurements of the flux of each component of HDF850.1, we assume that the relative flux in each component is 50 per cent, similar to what is seen in the far-IR continuum from PdBI. The procedure for performing the SED fits is also detailed in Section 3.3.2.

stellar continuum from HDF850.1 contributes substantially to the *F*444*W* flux that we measure for the southern component. For the northern component, the contribution from the stellar continuum seems to dominate the *F*444*W* flux given the absence of a clear line detection at its location.

3.3.2 SED modelling of UV + optical and far-IR light from HDF850.1

The *JWST* NIRcam observations presented here provide us with the first direct constraints on the stellar content of HDF850.1. We complement the photometry listed in Table 2 with the flux limits in *Herschel* bands, and the 1 mm flux density continuum reported for the two components of the system in Neri et al. (2014). We adopt the upper limits in *Herschel* bands from Walter et al. (2012) and perform our own analysis of the flux in the SPIRE bands using the MOPHONGO software (e.g. Labbé et al. 2006, 2010). Based on an attempted deblending of the low-resolution data at 250 μm with MOPHONGO, we measure no significant flux from HDF850.1, and hence adopt the 2σ upper limit from Liu et al. (2018) of 3.14 mJy. While there is a $\sim 5\sigma$ detection in the *Herschel* data at 350 and 500 μm, respectively, the low resolution makes it impossible to know the fraction of the flux that should be ascribed to each component of HDF850.1 or to a neighbour. Therefore, we use these values with asymmetric error bars such that the lower bound goes to 0, that is to say $11.6^{+2.2}_{-11.6}$ mJy and $11.3^{+2.8}_{-11.3}$, respectively. We note that the uncertainties we derive are consistent with that found in both Elbaz et al. (2011) and Liu et al. (2018). Additionally, as we are fitting the two components individually, we make the assumption that each component is responsible for 50 per cent of the flux in those bands and accordingly adjust the flux densities. We also make use of the 1 mm dust detections from Neri et al. (2014), namely 2.2 and 2.4 mJy for the northern and southern components, respectively, along with their 20 per cent uncertainties.

We model the SED of the northern and southern components of HDF850.1 using two different SED-fitting codes. This was done to better assess the large uncertainties expected from the small number of detections associated with this source. We make use of BAGPIPES (Carnall et al. 2018) as well as the high-redshift implementation of MAGPHYS (da Cunha, Charlot & Elbaz 2008; da Cunha et al. 2015). They both use the stellar populations based on Bruzual & Charlot's (2003) spectral libraries both assume energy balance between energy absorbed by dust in the rest-frame optical range and re-emitted in the far-IR. We fix the redshift at the Hα value and assume a delayed exponential function as the SFH. The best-fitting models are shown in Fig. 5. We infer the best fit of the free parameters and their uncertainties from the distribution of the posterior probabilities, interpolated at the 16 per cent, 50 per cent, and 84 per cent levels. Our best-fitting stellar masses, SFRs, far-IR luminosities, and dust attenuation for the two components of HDF850.1 are provided in Table 1.

The NIRCam observations sample the stellar continuum around the Balmer break, which lies at 2.1μm. Our fits suggest that both components of HDF850.1 are significantly dust reddened. The northern component of HDF850.1 appears slightly more massive and star forming, with a similar specific SFR, compared to the southern component. The precise flux measurements made possible thanks to our new NIRCam photometry pins down the stellar component of the fit; this however, combined with the energy balance assumption in the code, and the large uncertainties associated with the *Herschel* photometry of HDF850.1 as a whole, leads to the sizeable uncertainties in the dust continuum SED of HDF850.1. A better sampling of the IR continuum emission separately for the two components of HDF850.1 will be necessary to improve our characterization of the overall SED.

3.4 Extended galaxy structures surrounding HDF850.1

3.4.1 Redshift overdensity at $z \sim 5.2$ and comparison with earlier studies

Given the substantial clustering of other star-forming galaxies expected around massive galaxies like HDF850.1 and earlier results

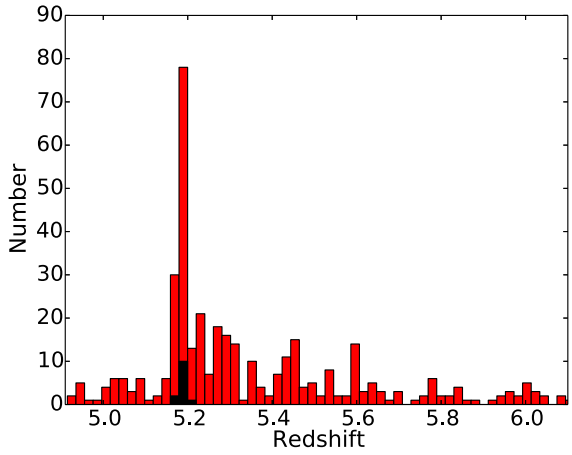

Figure 6. Redshift distribution of star-forming galaxies over the GOODS-North FRESCO field detected in Hα at $> 5\sigma$. Sources shown in black in the histogram were identified earlier as part of the spectroscopic sample of Walter et al. (2012) and Calvi et al. (2021). Clearly, there is strong evidence for a substantial spike in the redshift distribution of galaxies at $z = 5.17$–5.20, centred on the redshift of HUDF850.1. Twenty four of the sources in this redshift spike were identified earlier as part of the Arrabal Haro et al. (2018) analysis leveraging the SHARDS data set.

showing a significant overdensity of galaxies at $z \sim 5.2$ (Walter et al. 2012; Arrabal Haro et al. 2018; Calvi et al. 2021), it is logical to make use of the substantial number of sources with spectroscopic redshifts in the GOODS North field from FRESCO to investigate this matter more extensively.

Using the techniques described in Section 3.4.2, we constructed catalogues of Hα emitters over GOODS North FRESCO field. Fig. 6 shows the number of sources as a function of redshift, and it is clear there is a huge overdensity of sources at $z = 5.16$–5.20, with 100 sources found in that narrow-redshift interval. Walter et al. (2012) and Calvi et al. (2021) had both previously reported the same overdensity of galaxies at $z \sim 5.2$, adding 13 and 6 spectroscopic members, respectively. Analysis of the narrow-band SHARDS observations indicate 44 additional sources whose redshifts are consistent with lying in this overdensity (Arrabal Haro et al. 2018), but the redshift measurements from SHARDS are much less precise, i.e. $\Delta z \sim 0.07$, and so much more difficult to tie to distinct individual structures identified here.

Nineteen of the 100 Hα emitters that we identified in the redshift range $z = 5.16$ to 5.20 were previously flagged as probable members of the $z \sim 5.2$ overdensity by Walter et al. (2012), Arrabal Haro et al. (2018), and Calvi et al. (2021). These earlier studies appear to have been most efficient at identifying those member galaxies in the $z \sim 5.2$ overdensity with the highest Hα fluxes, likely as a result of these same sources showing more prominent Lyα emission lines for redshift determinations. Three out of the seven brightest Hα emitters (i.e. 43 per cent) were identified as part of earlier spectroscopic studies, as well as five out of the 14 brightest Hα emitters (i.e. 36 per cent). This compares with just 19 out of 100 sources (i.e. 19 per cent) that appeared in these earlier compilations.

Comparing our redshift measurements to those from Walter et al. (2012) and Calvi et al. (2021), the redshift measurements we derive are $\Delta z = -0.009 \pm 0.011$ lower in the mean than those in the literature. This is consistent with what we would expect for Lyα velocity offsets of 436 ± 582 km s^{-1}, in the general range of what has been found in many studies at $z \sim 3$–8 (e.g. Erb et al. 2014; Tang et al. 2023). Somewhat unexpectedly, only 6 of the 19 sources in the spectroscopic redshift catalogues of Walter et al. (2012) and Calvi et al. (2021) with coverage from FRESCO show up in our own catalogues of Hα emitters. Given the high completeness levels expected for our Hα-emitter searches, this suggests that previous spectroscopic samples were dominated by sources with high Lyα escape fractions.

There are three sources over the GOODS North field discussed by Walter et al. (2012) and Calvi et al. (2021) which have spectroscopic redshifts suggesting they are part of the prominent $z = 5.17$–5.20 overdensity discussed here, but which lie outside the $\sim$62 arcmin^2 FRESCO mosaic. These include a quasi-stellar object (QSO) at $z \sim 5.18$ (Barger et al. 2002) and two other galaxies SHARDS20008777 and a source at 12:36:00.0, 62:12:26.1. Nineteen of the plausible 50 sources with redshifts in the range $z = 5.12$–5.27 from Arrabal Haro et al. (2018) lie outside the FRESCO mosaic. Of the 31 sources from Arrabal Haro et al. (2018) which lie in the redshift range $z = 5.12$–5.27 and lie within the FRESCO mosaic, 17 are members of our spectroscopic sample of Hα emitters in the redshift range $z = 5.16$ to 5.20.

With 100 spectroscopic members of the overdensity at $z = 5.17$–5.20, this overdensity is particularly extreme. $\sim$28 per cent of the total number of $z = 5.0$–6.0 Hα emitters found over the HDF-North field lie in a $\Delta z \sim 0.03$ interval. This exceeds even the 45 galaxies present in $z \sim 5.4$ overdensity identified over the GOODS-South field (Helton et al. 2024) and also the 20 galaxy and 24 galaxy overdensities identified at $z \sim 6.19$ and ~ 6.33, respectively, over the J0100 + 2802 field by Kashino et al. (2023).

Given the much larger number of star-forming galaxies in the immediate vicinity of HDF850.1 than even present over the J0100 + 2802 field, this may suggest the halo masses associated with this overdensity may be even more extreme than the bright $z \sim 6.33$ QSO J0100 + 2802 that the EIGER program targeted. In particular, the $z = 5.17$–5.20 overdensity extends over the entire GOODS-North FRESCO field, i.e. a 18 cMpc × 18 cMpc area and 15 cMpc along the line of sight, which translates to a 4.8×10^3 cMpc^3 comoving volume. Assuming a similar efficiency for line emission across the redshift interval $z = 5.0$ to 6.0, this translates to an amplitude of $\delta_g + 1 = 8 \pm 1$ for the identified $z = 5.17$–5.20 overdensity.

Interestingly enough, the present overdensity is very similar in comoving size (17 cMpc × 20 cMpc × 26 cMpc and 17 cMpc × 20 cMpc × 36 cMpc), volume (6.7×10^3 cMpc^3 and 1.2×10^4 cMpc^3), and δ_g overdensity factors (4.8 ± 1.8 and 9.5 ± 2.0) to the overdensities at $z = 3.065$ and 3.095, respectively, identified over the SSA22 field by Steidel et al. (1998) and characterized in more detail by Topping et al. (2018).

3.4.2 *Extended galaxy structures around HDF850.1*

To gain insight into the structures that make up the overdensity at $z = 5.17$–5.20 and overdensities at $z = 5.20$–5.32, we constructed a list of candidate extended structures within the FRESCO GOODS-North volume based on our Hα-emitting catalogues. For this, we made use of the DBSCAN density-based clustering algorithm – which is part of the SCIKIT-LEARN (Pedregosa et al. 2011) to identify the structures. We set the minimum number of sources to define an overdensity to 3 and the linking length for the algorithm to 3.4 cMpc, which corresponds to $0.5\times$ the 1σ width ($\Delta z \sim 0.025$) of the $z = 5.17$–5.20 structure along the line of sight. As a result of the impact of a $\sigma_v \sim 700$km s^{-1} line-of-sight velocity for structures whose components sum to a mass $> 10^{13}$M$_\odot$, we expect structures to appear $\sim$7 cMpc

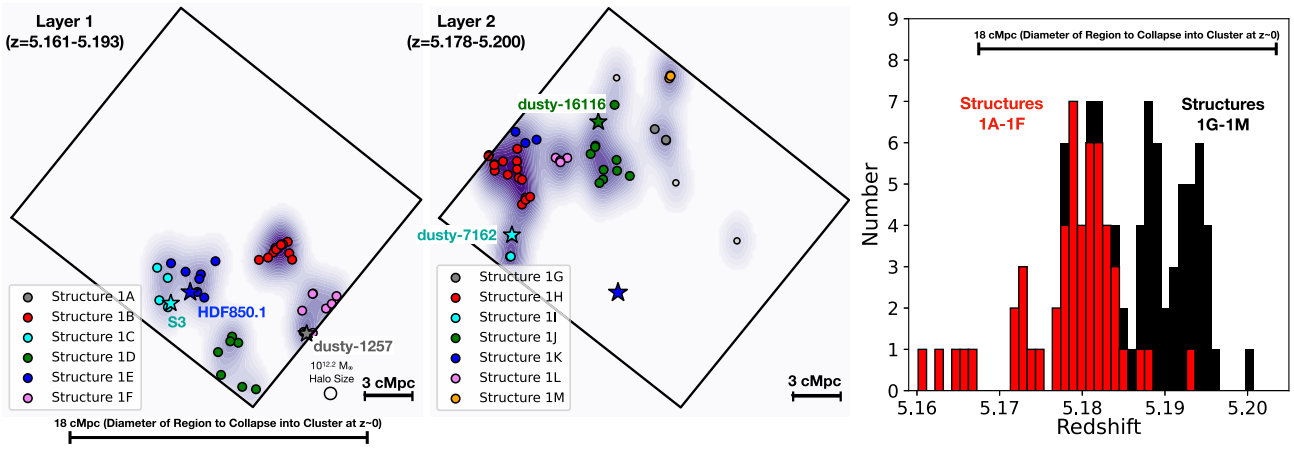

Figure 7. Spatial distribution of Hα emitters (left and centre panels) in the prominent overdensity at $z = 5.17$–5.20 in the GOODS-North FRESCO Field. The black lines enclose the area covered by the FRESCO *F444W* grism observations. Sources are shown in various colour filled circles depending on the extended structure each was tentatively identified to belong based on the redshift and spatial position on the sky. Smaller structures 1A–1F associated with the $z = 5.17$–5.20 overdensity are presented in the left panel, while the smaller structures 1G–1M are presented in the centre panel. The larger blue and smaller cyan star show the position of HDF850.1 and another dusty star-forming galaxy S3 (see Fig. 9) which appears to be part of the structure 1E and 1C, respectively. The grey, cyan, and green stars in the centre panel show the positions of three dusty galaxies dusty-1257, dusty-7162, and dusty-16116 identified in structures 1A, 1I, and 1J by Xiao et al. (2024). The horizontal bars towards the lower region of the left and centre panels indicate the comoving radii (3 cMpc) of the most extended structures identified here and the comoving diameter (18 cMpc: Chiang et al. 2017) of the regions of the universe at $z \sim 5.2$ that collapses into $> 10^{14}$ M$_\odot$ galaxy clusters by $z \sim 0$, respectively. The small open circle indicates the expected size of $10^{12.2}$M$_\odot$ haloes at $z \sim 5.2$, The rightmost panel shows the number of sources as a function of redshift. Sources in extended structures 1A–1F, shown as the red histogram, are distributed more towards the southern and western parts of the FRESCO GOODS-North field and mostly have redshifts between 5.165 and 5.185. Meanwhile, sources in structures 1G–1M, shown as the black histogram, are distributed more towards the eastern and northern parts of the FRESCO field and mostly have redshifts between 5.185 and 5.196. The horizontal bar shows the comoving length-scale (Chiang et al. 2017) of structures that collapse into $> 10^{14}$M$_\odot$ galaxy cluster by $z \sim 0$. The work of Chiang et al. (2017) suggest that the entire extended structure 1 identified here likely collapse into a single $> 10^{14}$M$_\odot$ galaxy cluster by $z \sim 0$.

longer along the line of sight. Accordingly, we divide the line-of-sight distances between sources by a factor of 2. For completeness, we also include several additional highly obscured galaxies identified by Xiao et al. (2024) to those identified using procedures from Section 2.3. These include GN10, which was previously identified as part of earlier work (Daddi et al. 2009; Riechers et al. 2020).

Using a linking length of 3.4 cMpc, we identify nine structures from $z = 5.15$ to 5.32 using DBSCAN. Not surprisingly, the most prominent structure lies at $z = 5.16$–5.20 and includes all Hα-emitting sources between $z = 5.16$ and 5.20. We also identify eight smaller structures at $z \sim 5.23$, 5.27, and 5.30. Given the number of sources in the $z = 5.17$–5.20 overdensity, we can also look at possible substructure within this overdensity. Again we do so using the DBSCAN density-based clustering algorithm but with a linking length that reduced by a factor of 2. With a linking length of 1.7 cMpc, we find 13 small structures embedded within the larger structure. The number of structures recovered with DBSCAN is sensitive to the linking length. Lengths of 1.0, 1.5, 2.0, and 2.5 cMpc result in the identification of 10, 13, 7, and 5 structures, respectively. Linking lengths smaller than 1.5 cMpc results in a decrease in the number of structures identified.

To help illustrate the 3D spatial distribution of galaxies and extended structures within this $z = 5.17$–5.20 overdensity, we have included Fig. 7, which shows six smaller structures we have identified at $z = 5.170$–5.185 (left panel) and seven smaller structures we have identified at $z = 5.185$–5.200 (centre panel). The rightmost panel shows the redshift distribution of sources in structures 1A–1F (red histogram) and structures 1G–1M (black histogram), pointing to the presence of a possible bimodality in the $z = 5.17$–5.20 overdensity. Additionally, the structures located in the lower redshift mode lie predominantly to the south and western parts of the FRESCO field, while structures in the higher redshift mode, lie predominantly to the north and east.

We have included a full list of the Hα emitters in the $z = 5.17$–5.20 overdensity in Table B1 from Appendix B. Galaxies which lie in some nearby overdensities at $z \sim 5.22$, ~ 5.27, and ~ 5.3 over the GOODS North FRESCO field are also presented in this table. In Appendix A, we present the spatial distribution in the plane of the sky of these slightly higher redshift overdensities. The spatial extent of the structures in these overdensities range from 1 to 4–5 cMpc in the plane of the sky, much less substantial than we see in the $z = 5.17$–5.20 overdensity that contains HDF850.1, which is the focus of this manuscript.

We include in Table 3 the central coordinates, mean redshift, nominal velocity dispersion, approximate radius, overdensity factor relative to the mean volume density of Hα emitters in the GOODS North FRESCO field, and number of member galaxies of these extended structures. The centre of each structure is provided both in right ascension and declination and offset from the center of the FRESCO GOODS North field. The median 1σ dispersion in redshift for the extended structures we identified is 0.0050, while the median velocity dispersion we find is 240^{+5}_{-21} km s^{-1}. If instead of considering structure 1 as a whole and instead consider the smaller structures that make it up, the median 1σ dispersion in redshift for structures is 0.0030, while the median velocity dispersion is 143^{+24}_{-13}km s^{-1}. This is 17 per cent larger and 30 per cent smaller, respectively, than the velocity dispersions Kashino et al. (2023) find, i.e. 212 and 197 km s^{-1}, for the overdensities in the J0100 + 2802 field at $z \sim 6.19$ and ~ 6.33, respectively. Not surprisingly, the dispersion in redshift and line-of-sight velocity is sensitive to whether we consider

Table 3. Extended structures identified From $z = 5.16$ to 5.31 in the FRESCO GOODS North field.[a]

ID	Structure centre RA	Dec.	$\Delta\alpha$ [cMpc]	$\Delta\delta$ [cMpc]	$z_{\rm mean}$	σ_v [km s^{-1}]	Radius [cMpc][b]	$1+\delta_g^c$	$\log_{10}\Sigma_i$ $M_{{\rm halo},i}/{\rm M}_\odot^d$	Number of members	Noteworthy members
1	12:36:51.32	62:14:03.3	0.9	−0.5	5.184	387	8.63	8	12.9	104	
1A	12:36:24.93	62:11:18.0	8.1	−6.9	5.165	126	0.27	–	11.8	4	dusty-1257
1B	12:36:31.23	62:13:34.9	6.4	−1.6	5.177	168	0.83	238	11.7	12	
1C	12:36:58.02	62:12:27.2	−0.8	−4.2	5.178	172	1.55	28	12.4	5	S3
1D	12:36:41.73	62:10:32.6	3.6	−8.6	5.180	114	2.06	32	11.8	7	
1E	12:36:50.76	62:12:47.7	1.1	−3.4	5.183	130	1.81	45	12.2	8	HDF850.1
1F	12:36:21.71	62:12:03.4	9.0	−5.1	5.183	161	1.51	42	11.3	7	
1G	12:36:41.61	62:16:43.9	3.6	5.6	5.188	79	0.54	–	11.3	3	
1H	12:37:17.24	62:15:41.9	−6.0	3.3	5.189	130	1.63	79	12.1	16	
1I	12:37:11.98	62:13:14.6	−6.0	−1.3	5.191	143	0.58	–	11.7	4	dusty-7162
1J	12:36:55.01	62:16:16.8	−0.0	4.6	5.191	131	1.96	38	11.5	12	dusty-16116
1K	12:37:13.64	62:16:41.1	−5.1	5.5	5.194	40	1.52	–	11.3	3	
1L	12:37:05.41	62:16:05.6	−2.8	4.2	5.194	40	0.54	–	11.0	4	
1M	12:36:39.79	62:18:22.9	4.1	9.5	5.194	60	0.26	–	11.4	3	
2	12:37:09.59	62:13:16.2	−4.0	−2.3	5.220	245	3.64	6	12.2	18	
3	12:37:03.91	62:15:47.2	−2.5	3.5	5.229	219	2.86	6	10.8	5	
4	12:36:32.30	62:15:17.2	6.2	2.4	5.269	249	2.09	3	11.6	17	
5	12:36:55.05	62:13:23.2	−0.1	−2.0	5.295	448	3.12	–	11.2	3	
6	12:36:26.44	62:14:17.7	7.8	0.1	5.300	167	1.97	23	12.5	10	
7	12:36:30.00	62:17:33.8	6.8	7.8	5.301	67	0.86	–	10.6	3	
8	12:37:20.59	62:15:31.5	−7.1	3.0	5.304	240	2.43	7	11.7	5	
9	12:36:38.67	62:09:45.6	4.5	−10.5	5.308	216	1.79	–	10.8	3	

Notes. [a]These structures are presented in Fig. 7 and Fig. A1. Structures 1A–1M represent smaller structures contained within the especially large overdensity at $z = 5.17$–5.20. The smaller structures were identified with DBSCAN using a smaller linking length. See Section 3.4.2.

[b] Estimated using equation (4). Since the expected sizes of collapsed halos with masses of $10^{12.0}$ and $10^{12.2}{\rm M}_\odot$ are 0.3 and 0.4 cMpc, respectively, this suggests that the identified overdensities are composed of extended structure, rather than represent galaxies within a single halo.

[c] This is the estimated amplitude of the overdensity of Hα emitters in the cylindrical volume enclosed within the estimated radius of the structure and a $|\Delta z| < 2\sigma_v/c$ relative to Hα emitters over the entire FRESCO GOODS-North volume.

[d] Four haloes with mass $10^{12.0}{\rm M}_\odot$ and one halo mass with mass $10^{12.2}{\rm M}_\odot$ are expected within the FRESCO GOODS North $z = 5.0$−6.0 volume.

substantial overdensities as single structures or as an ensemble of smaller structures.

Following Long et al. (2020) and Calvi et al. (2021), we also use the stellar masses of the member galaxies to estimate the integrated halo masses of the extended structures that host the galaxies in the extended structures. We do so by computing the total stellar mass we estimate from the member galaxies and then supposing an integrated star formation efficiency of 5 per cent based on detailed studies comparing the galaxy stellar mass functions to the halo mass functions (Behroozi & Silk 2018), but we note that detailed studies (McLeod et al. 2021; Stefanon et al. 2021) of the ratio of the stellar mass to halo mass density from galaxy stellar mass functions at $z \sim 0$–10 integrated down to $10^8 M_\odot$ give factors between 0.5 per cent to 2 per cent. We make use of the masses from Naidu et al. (in preparation) SED fits with PROSPECTOR – except for the sources in the optically faint samples of Xiao et al. (2024). The derived integrated halo masses range from $10^{10.6}$ and $10^{12.6} M_\odot$. Not surprisingly, HDF850.1 and GN10 lie in the halos that belong to the structures with the highest integrated halo masses. Assuming a survey area of ∼62 arcmin^2 and $\Delta z \sim 1$ volume ($\sim 2\times10^5$ cMpc^3), we estimate that the GOODS North FRESCO volume should contain approximately one $10^{12.2} M_\odot$ halo. For this calculation, we made use of the public halo mass function calculator HMFcalc by Murray, Power & Robotham (2013) adopting a Planck Collaboration VI (2020) cosmology.

The radius of each extended structure $R_{\rm structure}$ is computed using the standard formula from Heisler, Tremaine & Bahcall (1985) used in computing dynamical masses of galaxy clusters based on a discrete number of galaxies with measured positions and line-of-sight velocities:

$$R_{\rm structure} = \frac{\pi N}{2\Sigma_{i<j} \frac{1}{R_{\perp ij}}} \quad (4)$$

where N is the number of galaxies in an extended structure and $R_{\perp ij}$ is the projected distance in the plane of the sky between galaxy i and galaxy j.

We also estimate overdensities for the extended structure we identified as part of Table 3 by comparing the volume density of Hα emitters within the estimated radius and a $|\Delta z| < 2\sigma_z$ redshift width of an extended structure to that found between $z = 5.0$ to 6.0 for the GOODS-North FRESCO field as a whole. We compute overdensity factors between 3 and 238, far in excess of the linear regime. Based on the volume density of Hα emitters we find in the GOODS North FRESCO volume, i.e. 1.6×10^{-3} cMpc^{-3}, we can estimate a nominal bias for this population assuming abundance matching and find an average bias factor of ∼4.7 using the Trenti & Stiavelli (2008) 'cosmic variance' calculator. Adjusting for this bias factor, this is suggestive of overdensities in the matter distribution ranging from 1 to 50, which is in excess of ≈1 for the linear regime but less than 200× overdensities expected for completely collapsed structures.

It is interesting to ask whether we would expect protoclusters to be present over the FRESCO fields and indeed within the GOODS North FRESCO field. Given that clusters generally have a mass of at least $10^{14} M_\odot$ (e.g. Kravtsov & Borgani 2012) at $z \sim 0$, we can use abundance matching to estimate whether the FRESCO volume contains any such objects. Using the halo mass functions from HMFcalc, we estimate the FRESCO GOODS-North volume to include four such clusters with mass $10^{14.0} M_\odot$ and one cluster reaching a mass of $10^{14.4} M_\odot$.

3.4.3 Comparison of structure sizes to the expected sizes of protoclusters

We can compare the size of the extended structures we find to that expected from the detailed study of protocluster growth (Chiang et al. 2017) making use of several semi-analytic galaxy formation models (Guo et al. 2013; Henriques et al. 2015) applied to the Millennium simulations (Springel et al. 2005). Chiang et al. (2017) present both the comoving sizes of collapsed protoclusters at various redshifts and the sizes of cosmic volumes that will collapse into $> 10^{14} M_\odot$ galaxy clusters by $z \sim 0$. Of relevance, Chiang et al. (2017) find protoclusters to have a comoving radius of ∼9 cMpc at $z \sim 5.2$, implying overdense structures to extend over a comoving distance of ∼18 cMpc, very similar to the spatial extent of the overdensities we have identified over the GOODS North FRESCO field (Fig. 7). Chiang et al. (2017) suggest that the entire $z = 5.17$–5.20 structure here will likely collapse into a single $> 10^{14} M_\odot$ galaxy cluster by $z \sim 0$.

We estimate that the halo masses of the most massive collapsed halo in those extended structures would be $10^{12.0}$ and $10^{12.2} M_\odot$, respectively, at $z \sim 5.2$. Assuming that average overdensity factor in the collapsed halos is 200, the size of the halos would be 0.3 and 0.4 cMpc at $z \sim 5.2$, i.e. 8 to 13 arcsec in the plane of the sky. In computing a radius of the identified structures, the above equation gives greater weight to galaxy pairs that have smaller separations. The fact that many of these extended structures have computed sizes not especially larger than 0.4 cMpc suggests that at least a few of the member galaxies in the extended structures are part of the same haloes.

3.4.4 Characteristics of galaxies in the $z = 5.17$–5.20 overdensity versus those outside

To put the extreme properties of HDF850.1 in context, we use the SED-fitting code PROSPECTOR (Leja et al. 2017; Johnson et al. 2021) to derive galaxy properties from our extensive spectroscopically confirmed sample of galaxies in FRESCO GOODS-North. Our PROSPECTOR fits use FSPS with the MIST stellar models. We do not fit for redshift and set it to the derived $z_{\rm grism}$ value infered by our pipeline using GRIZLI. Along with the photometry, fluxes from emission lines identified in the grism 1D spectra are also used as an input. We make use of PROSPECTOR's more flexible non-parametric SFH with eight bins evenly separated in lookback time with a 'continuity' prior for smoother SFH. The output catalogue contains all sources detected in the detection image that were visually inspected by at least one member of the FRESCO team along with the inferred properties from SED-fitting such as the retained stellar mass $M_\star$, UV slope β, star formation rates, SFR or age at 50 per cent of the total stellar mass.

To highlight the distinct properties galaxies may have within the overdensity or its structures and outside of it, we compare two samples. One contains all the galaxies in the $z = 5.17$–5.20 overdensity that have been identified as being part of a structure ('in' with 40 sources), while the second sample contains all the remaining galaxies from $z = 4.9$ to 5.5 not identified in such structures ('out' with 86) and also excluding the redshift bin $z = 5.17$–5.20. We also apply a magnitude cut of 27 AB mag in $F182M$. While this will limit our inferences to galaxies intrinsically brighter than −20 mag, this choice was made to alleviate the uncertainties on the inferred parameters from faint sources – particularly for stellar masses – and avoid a bias towards strong Hα emitters only. We report the output of the PROSPECTOR fits for these two samples with kernel density estimate (KDE) plots as shown in Fig. 8. We also compare

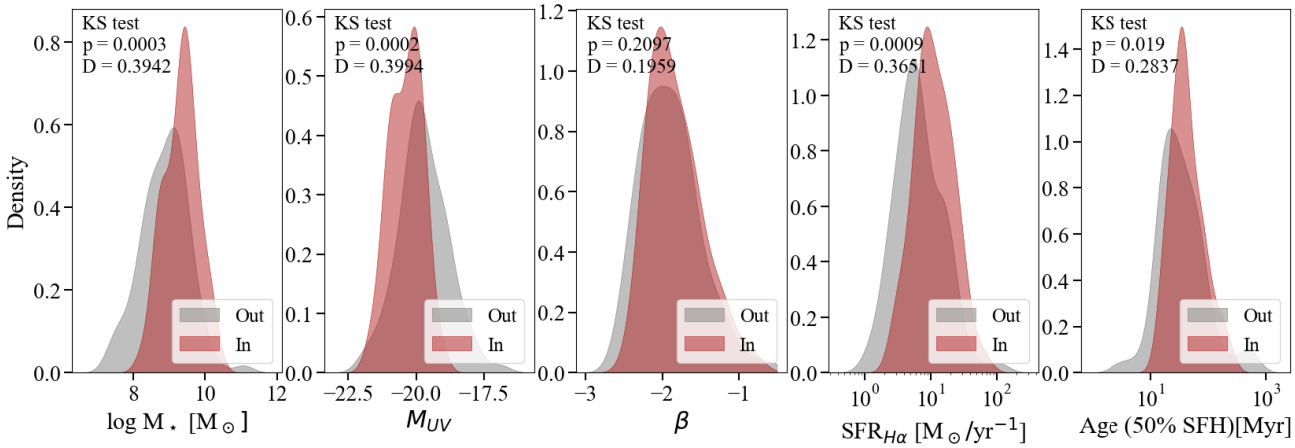

Figure 8. KDE density plots showing the comparison of PROSPECTOR-inferred galaxy properties for sources inside and outside of the overdensity. The 'in' sample (red) contains 47 sources between redshifts $z = 5.17$–5.20 in the overdensity and identified as part of extended structures, while the 'out' sample (grey) contains 86 sources at redshift $z = 4.9$–5.5 excluding the overdensity redshift bin and the structures identified with the method detailed in Section 3.4.2. Shown in each panel are differences in the fractional cumulative distribution and associated probability that the two distributions are consistent using a KS test. The stellar masses, *UV* luminosities, and SFRs for galaxies inside the overdensities show a clear shift to higher values than galaxies outside the overdensities.

SFRs inferred from Hα using equation (1). We use the Hα flux corrected for dust attenuation with the empirical relation linking it to β slopes from Shivaei et al. (2020). Finally, we use a two-sample Kolmogorov–Smirnov (KS) test to comment on the dissimilarities in our selection of sources.

Based on the sizes of our two samples, we require a critical *D*-value of 0.3311 to demonstrate at 99.5 per cent confidence ($\alpha = 0.005$) that the distributions of the properties for sources inside and outside overdensities are different. While we do not find a clear differences (at 99.5 per cent confidence) in the distributions for β slopes and ages at 50 per cent of the SFH, the *D*- and *p*-values for the masses and ages show clear differences between the two populations of galaxies at this redshift. Our results suggest that the galaxies in the overdensity are more evolved, more massive and with higher SFRs than the galaxies outside of these structures. The median stellar mass $M_\star$ in the overdensity is $\sim 2.5 \times 10^9 M_\odot$ versus $\sim 8 \times 10^8 M_\odot$ for the galaxies outside, a factor of ∼3 difference. Earlier work by Steidel et al. (2005) had shown that the masses and ages of galaxies in a similarly prominent (i.e. $\delta_g \sim 7$) overdensity at $z = 2.3$ were twice as high as those outside the overdensity in line with our results.

More evidence from FRESCO for the most extreme sources being found in overdense environments can be found in the Xiao et al. (2024) Hα selection of highly obscured sources over the GOODS North field. In particular, the five $z = 4.9$–6.6 sources with the highest estimated stellar masses and SFRs all lie within the overdensities at $z \sim 5.16$–5.20 and ~ 5.30. We show one of these sources in Fig. 9, a neighbour to HDF850.1 which was given source ID S3. That source has a redshift $z = 5.179$ derived from the detection of both Hα ($> 20\sigma$) and the [S II]$_{6719,6730}$ doublet ($\sim 9\sigma$: Xiao et al. 2024). Remarkably, this source shows even more extreme stellar masses and SFRs than HDF850.1 (Xiao et al. 2024). Xiao et al. (2024) present a much larger sample of obscured, Hα emitters at $z > 5$, leveraging the FRESCO NIRCam grism data to derive spectroscopic redshifts. The existence of large numbers of obscured galaxies with detectable Hα emission may arise because of prevalent merging activity amongst the brightest far-IR sources (e.g. Clements et al. 1996; Tacconi et al. 2008) and the possibility that the merging activity could create less obscured sightlines by which Hα photons could escape from galaxies (e.g. Le Reste et al. 2024). One of the components in a merging system might also be subject to substantially less dust obscuration, which would also enhance the detectability of IR luminous sources.

4 SUMMARY

In this paper, we present the detection of a 13σ Hα line for HDF850.1 in the NIRCam *F*444*W* grism observations over the GOODS North field from FRESCO (Oesch et al. 2023), recovering a redshift of 5.188±0.001. Detection of Hα in HDF850.1 is particularly noteworthy, given how obscured star formation from the source is. HDF850.1 was one of the first submm galaxies to be identified with SCUBA (Hughes et al. 1998) and evaded efforts to pin down its redshift for >10 yr until the PdBI secured the detection of [C II] and various CO lines from a spectral scan (Walter et al. 2012).

In addition, HDF850.1 is clearly detected in the *F*444*W* imaging observations available over the source with NIRCam, with the emission segregated into a distinct northern and southern component. These two distinct components were also evident in the earlier observations of [C II] from HDF850.1 with PdBI (Neri et al. 2014). Modelling the SEDs of the two components of HDF850.1 based on the available *HST* + NIRCam *F*182*M*, *F*210*M*, and *F*444*W* imaging observations, we find a much higher SFR, stellar mass, and dust obscuration for the northern component than the southern component.

The majority of the Hα emission for HDF850.1 appears consistent with originating from the southern component, not only due to the spatial localization of the emission but also due to its showing a very similar $\Delta v \sim 130$ km s^{-1} velocity offset to that seen in the southern component from [C II] emission (Neri et al. 2014). Comparison of the SFR inferred from the observed Hα emission with that seen from [C II] is suggestive of the Hα emission from the southern component being 93±3 per cent attenuated and the northern component >98 per cent attenuated.

Leveraging redshift determinations possible from the FRESCO NIRCam grism observations in *F*444*W* over the GOODS North field, we note the existence of 100 galaxies in total in the $z = 5.17 - 5.20$ interval, indicative of a huge 8× overdensity of galaxies in that redshift interval relative to the $z = 5.0 - 6.0$ population of Hα

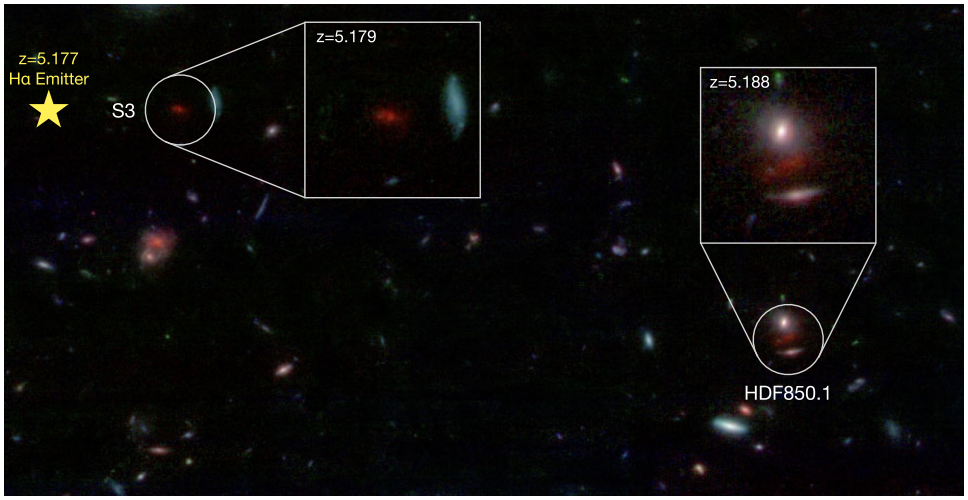

Figure 9. Upper panels: colour composite image of another highly obscured star-forming source S3 at $z = 5.179$ which is part of the same z=5.17–5.20 overdensity as HDF850.1, as seen in a false colour image (60 arcsec × 30 arcsec) made with the *JWST* NIRCam *F*182*M*, *F*210*M*, and *F*444*W* data. The redshift $z = 5.179$ of this source is based on the detection of both Hα ($> 20\sigma$) and the [S II]$_{6719,6730}$ doublet ($\sim 9\sigma$) in the FRESCO grism data. Another Hα emitter (ID 3946) at $z = 5.177$ from the same extended structure (indicated with a star) also lies within this same footprint and could reside in the same dark matter halo as S3 (being separated by 7 arcsec [or 0.26 cMpc] in the plane of the sky). Redshift measurements have been obtained for a large number of other highly obscured galaxies over the ∼124 arcmin^2 FRESCO mosaic using detected Hα lines (Xiao et al. 2024), with typical S/N's of >10 for the sources with the highest inferred SFRs. The detection of Hα line emission from sources like HDF850.1 and S3 – and many similarly dust-obscured and high-SFR sources – shows the huge potential wide-area NIRCam grism observations have for mapping the build-up of massive, dust-enshrouded star-forming galaxies in the early universe.

emitters we see over GOODS North. Earlier work by Walter et al. (2012), Arrabal Haro et al. (2018), and Calvi et al. (2021) had previously demonstrated the existence of a substantial overdensity around HDF850.1, but with a much smaller number of spectroscopically confirmed sources than we find as part of this study.

Taking advantage of both the spatial and redshift information we have of galaxies in the $z = 5.17$–5.20 and slightly higher redshift ($z = 5.22$–5.31) overdensities, we have used the DBSCAN density-based clustering algorithm to identify 9 more extended structures using a linking length of 3.4 cMpc and decomposed the largest structure at $z = 5.17$–5.20 into 13 smaller structures using a smaller linking length (1.7 cMpc). For each structure, we have computed radii, masses, velocity dispersions. The median 1σ dispersion found the more extended structures is 0.0050 in redshift and 240^{+5}_{-21} km s^{-1} in $v_{\rm los}$. If we consider smaller structures within the $z = 5.17$–5.20 overdensity, the 1σ dispersion in redshift and in $v_{\rm los}$ becomes 0.0030 and 143^{+24}_{-13} km s^{-1}. This is 17 per cent larger and 30 per cent smaller, respectively, than what Kashino et al. (2023) find for the extended structures in the J0100 + 2802 field at $z \sim 6.19$ and ~ 6.33.

Interestingly, the comoving physical size of the extended structures we find around HDF850.1 extend over a 18 cMpc × 18 cMpc × 15 cMpc volume, very similar to the ∼18 cMpc physical size, Chiang et al. (2017) expect for protoclusters based on an analysis of various semi-analytic galaxy formation results building on the Millennium simulation (Springel et al. 2005: Section 3.4.3). The link to the $z = 5.17$–5.20 overdensity being the progenitor to a $> 10^{14}$M$_\odot$ $z \sim 0$ galaxy cluster is further strengthened by noting that within the FRESCO GOODS North volume we would expect four $> 10^{14}$M$_\odot$ clusters and one $> 10^{14.4}$M$_\odot$ cluster to form by $z \sim 0$.

Additionally, we have made a systematic comparison of galaxy masses, SFRs, *UV* luminosities, ages, and apparent dust extinctions inside the $z = 5.17$–5.20 overdensity to that outside the $z = 5.17$–5.20 overdensity and other overdensities in the field. We find strong evidence ($> 3\sigma$) that galaxies inside the overdensities have higher stellar masses, SFRs, and *UV* luminosities than those outside these overdensities. This conclusion is strengthened by the inclusion of optically faint, massive, high-SFR dust-obscured galaxies at $z = 5.0$–6.0, almost all of which lie inside some overdensity within the GOODS North.

In the future, it should be possible to significantly expand the number of dusty star-forming galaxies identified in the $z > 5$ universe thanks to ongoing NIRCam grism observations from EIGER (Kashino et al. 2023), ASPIRE (Wang et al. 2023), a new NIRCam grism program from MIRI GTO team over GOODS South (program ID 4549), as well as deeper NIRCam grism observations approved over a deep NIRCam parallel field (program ID 4540) and various HFF clusters (program IDs 2883, 3516, and 3538). Of course, to obtain the strongest constraints, a much wider area NIRCam program will be essential, and so it is exciting that in cycle 3, there will be the COSMOS-3D program obtaining grism data over a 1200 arcmin^2 area over the COSMOS field (Kakiichi et al. 2024). This program will be especially useful for further explorations such as the present one leveraging far-IR observations available from the ex-MORA program over the COSMOS field (Casey et al. 2021) and CHAMPS program (2023.1.00180.L, PI: Faisst) covering $\gtrsim$50 per cent of the NIRCam grism mosaic.

ACKNOWLEDGEMENTS

We are grateful to Roberto Neri and collaborators for providing us with spatially resolved information on both the dust-continuum and [C II] line emission from their high spatial resolution PdBI observations. This project was made possible in part by the Leiden University Fund/Bouwens Astrophysics Fund. RJB acknowledges support from NWO grants 600.065.140.11N211 (vrij competitie) and TOP grant TOP1.16.057. The Cosmic Dawn Center (DAWN) is funded by the Danish National Research Foundation under grant no. 140. Cloud-based data processing and file storage for this work is provided by the AWS Cloud Credits for Research

program. Support for this work was provided by NASA through grant JWST-GO-01895 awarded by the Space Telescope Science Institute, which is operated by the Association of Universities for Research in Astronomy, Inc., under NASA contract NAS 5–26555. RPN acknowledges funding from *JWST* programs GO-1933 and GO-2279. Support for this work was provided by NASA through the NASA Hubble Fellowship grant HST-HF2-51515.001-A awarded by the Space Telescope Science Institute, which is operated by the Association of Universities for Research in Astronomy, Incorporated, under NASA contract NAS5-26555. MS acknowledges support from the CIDEGENT/2021/059 grant, from project PID2019-109592GB-I00/AEI/10.13039/501100011033 from the Spanish Ministerio de Ciencia e Innovación – Agencia Estatal de Investigación. This study forms part of the Astrophysics and High Energy Physics programme and was supported by MCIN with funding from European Union NextGenerationEU (PRTR-C17.I1) and by Generalitat Valenciana under the project n. ASFAE/2022/025. RAM acknowledges support from the ERC Advanced Grant 740246 (Cosmic_Gas) and the Swiss National Science Foundation through project grant 200020_207349.

This work is based on observations made with the NASA/ESA/CSA *JWST*. The data were obtained from the Mikulski Archive for Space Telescopes at the Space Telescope Science Institute, which is operated by the Association of Universities for Research in Astronomy, Inc., under NASA contract NAS 5–03127 for *JWST*. These observations are associated with program no. 1895.

This paper made use of several publicly available software packages. We are indebted to the respective authors for their work: IPYTHON (Pérez & Granger 2007), MATPLOTLIB (Hunter 2007), NUMPY (Oliphant 2006), SCIPY (Virtanen et al. 2020), JUPYTER (Kluyver et al. 2016), ASTROPY (Astropy Collaboration 2013, 2018), GRIZLI (v1.7.11; Brammer 2018; Brammer et al. 2022), EAZY (Brammer, van Dokkum & Coppi 2008), and SExTRACTOR (Bertin & Arnouts 1996).

DATA AVAILABILITY

All data used here are from the *JWST* Cycle 1 (GO 1895) and publicly available from the Barbara A. Mikulski Archive for Space Telescopes (MAST: https://mast.stsci.edu). Data were reduced with the publicly-available code GRIZLI (https://grizli.readthedocs.io). The reduced imaging data is available at https://s3.amazonaws.com/grizli-v2/JwstMosaics/v7/index.html or through MAST: https://archive.stsci.edu/hlsp/fresco.

REFERENCES

Álvarez-Márquez J. et al., 2023, A&A, 671, A105
Arrabal Haro P. et al., 2018, MNRAS, 478, 3740
Astropy Collaboration, 2013, A&A, 558, A33
Astropy Collaboration, 2018, AJ, 156, 123
Barger A. J., Cowie L. L., Brandt W. N., Capak P., Garmire G. P., Hornschemeier A. E., Steffen A. T., Wehner E. H., 2002, AJ, 124, 1839
Behroozi P., Silk J., 2018, MNRAS, 477, 5382
Bertin E., Arnouts S., 1996, A&AS, 117, 393
Béthermin M. et al., 2020, A&A, 643, A2
Bouwens R. J. et al., 2021, AJ, 162, 47
Bouwens R. J. et al., 2022, ApJ, 931, 160
Brammer G., 2018, Gbrammer/Grizli: Preliminary Release, Zenodo, available at: https://zenodo.org/records/1146905
Brammer G. B., van Dokkum P. G., Coppi P., 2008, ApJ, 686, 1503
Brammer G., Strait V., Matharu J., Momcheva I., 2022, grizli, Zenodo, available at: https://doi.org/10.5281/zenodo.6672538
Bruzual G., Charlot S., 2003, MNRAS, 344, 1000
Calvi R., Dannerbauer H., Arrabal Haro P., Rodríguez Espinosa J. M., Muñoz-Tuñón C., Pérez González P. G., Geier S., 2021, MNRAS, 502, 4558
Carnall A. C., McLure R. J., Dunlop J. S., Davé R., 2018, MNRAS, 480, 4379
Casey C. M. et al., 2021, ApJ, 923, 215
Chabrier G., 2003, PASP, 115, 763
Chiang Y.-K., Overzier R. A., Gebhardt K., Henriques B., 2017, ApJ, 844, L23
Clements D. L., Sutherland W. J., McMahon R. G., Saunders W., 1996, MNRAS, 279, 477
Covelo-Paz A. et al., 2024, preprint (arXiv:2409.17241)
Cowie L. L., Barger A. J., Wang W. H., Williams J. P., 2009, ApJ, 697, L122
da Cunha E., Charlot S., Elbaz D., 2008, MNRAS, 388, 1595
da Cunha E. et al., 2015, ApJ, 806, 110
Daddi E., Dannerbauer H., Krips M., Walter F., Dickinson M., Elbaz D., Morrison G. E., 2009, ApJ, 695, L176
Davidzon I. et al., 2017, A&A, 605, A70
Dayal P. et al., 2022, MNRAS, 512, 989
Díaz-Santos T. et al., 2013, ApJ, 774, 68
Dojčinović I., Kovačević-Dojčinović J., Popović L. Č., 2023, Adv. Space Res., 71, 1219
Downes D. et al., 1999, A&A, 347, 809
Dunlop J. S. et al., 2004, MNRAS, 350, 769
Elbaz D. et al., 2011, A&A, 533, A119
Erb D. K. et al., 2014, ApJ, 795, 33
Faisst A. L. et al., 2020, ApJS, 247, 61
Freeman W. R. et al., 2019, ApJ, 873, 102
Giavalisco M. et al., 2004, ApJ, 600, L93
Grogin N. A. et al., 2011, ApJS, 197, 35
Guo Q., White S., Angulo R. E., Henriques B., Lemson G., Boylan-Kolchin M., Thomas P., Short C., 2013, MNRAS, 428, 1351
Harikane Y. et al., 2022, ApJ, 929, 1
Heisler J., Tremaine S., Bahcall J. N., 1985, ApJ, 298, 8
Helton J. M. et al., 2024, ApJ, 962, 124
Henriques B. M. B., White S. D. M., Thomas P. A., Angulo R., Guo Q., Lemson G., Springel V., Overzier R., 2015, MNRAS, 451, 2663
Hughes D. H. et al., 1998, Nature, 394, 241
Hunter J. D., 2007, Comput. Sci. Eng., 9, 90
Illingworth G. et al., 2016, preprint (arXiv:1606.00841)
Johnson B. D., Leja J., Conroy C., Speagle J. S., 2021, ApJS, 254, 22
Kakiichi K. et al., 2024, COSMOS-3D: A Legacy Spectroscopic/Imaging Survey of the Early Universe, JWST Proposal. Cycle 3, ID. #5893
Kashino D., Lilly S. J., Matthee J., Eilers A.-C., Mackenzie R., Bordoloi R., Simcoe R. A., 2023, ApJ, 950, 66
Kennicutt R. C., Evans N. J., 2012, ARA&A, 50, 531
Kewley L. J., Dopita M. A., Leitherer C., Davé R., Yuan T., Allen M., Groves B., Sutherland R., 2013, ApJ, 774, 100
Kluyver T. et al., 2016, in Fernando L., Birgit S., eds, Positioning and Power in Academic Publishing: Players, Agents and Agendas. IOS Press, Fairfax, Virginia, p. 87
Koekemoer A. M. et al., 2011, ApJS, 197, 36
Kravtsov A. V., Borgani S., 2012, ARA&A, 50, 353
Kroupa P., Weidner C., 2003, ApJ, 598, 1076
Labbé I., Bouwens R., Illingworth G. D., Franx M., 2006, ApJ, 649, L67
Labbé I. et al., 2010, ApJ, 716, L103
Le Fèvre O. et al., 2020, A&A, 643, A1
Le Reste A. et al., 2024, MNRAS, 528, 757
Leja J., Johnson B. D., Conroy C., van Dokkum P. G., Byler N., 2017, ApJ, 837, 170
Liu D. et al., 2018, ApJ, 853, 172
Long A. S. et al., 2020, ApJ, 898, 133
Madau P., Dickinson M., 2014, ARA&A, 52, 415
Matthee J. et al., 2024, ApJ, 963, 129
McLeod D. J., McLure R. J., Dunlop J. S., Cullen F., Carnall A. C., Duncan K., 2021, MNRAS, 503, 4413
Murray S. G., Power C., Robotham A. S. G., 2013, Astron. Comput., 3–4, 23
Neri R., Downes D., Cox P., Walter F., 2014, A&A, 562, A35
Oesch P. A. et al., 2023, MNRAS, 525, 2864

Oke J. B., Gunn J. E., 1983, ApJ, 266, 713
Oliphant T. E., 2006, Guide to NumPy. Trelgol Publishing
Pedregosa F. et al., 2011, J. Mach. Learn. Res., 12, 2825
Peng C. Y., Ho L. C., Impey C. D., Rix H.-W., 2002, AJ, 124, 266
Pérez F., Granger B. E., 2007, Comput. Sci. Eng., 9, 21
Perrin M. D., Sivaramakrishnan A., Lajoie C.-P., Elliott E., Pueyo L., Ravindranath S., Albert L., 2014, in Proc. SPIE Conf. Ser. Vol. 9143, SpaceTelescopes and Instrumentation 2014: Optical, Infrared, and MillimeterWave. SPIE, Bellingham, p. 91433X
Planck Collaboration VI, 2020, A&A, 641, A6
Reddy N. A., Steidel C. C., Erb D. K., Shapley A. E., Pettini M., 2006, ApJ, 653, 1004
Reddy N. A., Steidel C. C., Pettini M., Adelberger K. L., Shapley A. E., Erb D. K., Dickinson M., 2008, ApJS, 175, 48
Reddy N. A., Topping M. W., Sanders R. L., Shapley A. E., Brammer G., 2023, ApJ, 948, 83
Richards E. A., 1999, ApJ, 513, L9
Riechers D. A. et al., 2020, ApJ, 895, 81
Robertson B. E., 2022, ARA&A, 60, 121
Schaerer D. et al., 2020, A&A, 643, A3
Shapley A. E. et al., 2015, ApJ, 801, 88
Shivaei I. et al., 2020, ApJ, 899, 117
Smail I. et al., 2021, MNRAS, 502, 3426
Springel V. et al., 2005, Nature, 435, 629
Stefanon M., Bouwens R. J., Labbé I., Illingworth G. D., Gonzalez V., Oesch P. A., 2021, ApJ, 922, 29
Steidel C. C., Adelberger K. L., Dickinson M., Giavalisco M., Pettini M., Kellogg M., 1998, ApJ, 492, 428
Steidel C. C., Adelberger K. L., Shapley A. E., Erb D. K., Reddy N. A., Pettini M., 2005, ApJ, 626, 44
Sun F. et al., 2024, ApJ, 961, 69
Tacconi L. J. et al., 2008, ApJ, 680, 246
Tang M. et al., 2023, MNRAS, 526, 1657
Topping M. W., Shapley A. E., Steidel C. C., Naoz S., Primack J. R., 2018, ApJ, 852, 134
Trenti M., Stiavelli M., 2008, ApJ, 676, 767
Virtanen P. et al., 2020, Nat. Methods, 17, 261
Wagg J., Hughes D. H., Aretxaga I., Chapin E. L., Dunlop J. S., Gaztañaga E., Devlin M., 2007, MNRAS, 375, 745
Walter F. et al., 2012, Nature, 486, 233
Wang F. et al., 2023, ApJ, 951, L4
Weiner B. J., AGHAST Team, 2014, in American Astronomical Society Meeting Abstracts #223, p. 227.07
Whitaker K. E., Pope A., Cybulski R., Casey C. M., Popping G., Yun M. S., 2017, ApJ, 850, 208
Whitaker K. E. et al., 2019, ApJS, 244, 16
Xiao M. et al., 2024, Nature, 635, 311

SUPPORTING INFORMATION

Supplementary data are available at *MNRAS* online.

appendix_B_table.txt

Please note: Oxford University Press is not responsible for the content or functionality of any supporting materials supplied by the authors. Any queries (other than missing material) should be directed to the corresponding author for the article.

APPENDIX A: EXTENDED GALAXY STRUCTURES AT z∼5.22–5.31

For completeness and as an illustration of the extended galaxy structures that exist at redshift just above the prominent $z = 5.17$–5.20 overdensity. Similar to Fig. 7 from the main text, we show in Fig. A1 the spatial distribution of galaxies in the galaxy overdensities at the slightly higher redshifts of $z \sim 5.23$, ~ 5.27, and ~ 5.30 for context. As in the main text, we have segregated sources in the overdensities into different structures using the same approach as described in Section 3.4.2.

While in some cases these overdensities consist of just a single group of ∼3–10 galaxies lying within 1 cMpc of each other (e.g. structures 9 and 15), in other cases the overdensities extend over larger (∼3–5 cMpc) scales. However, even for the most extended structures in these overdensities, galaxies in these overdensities are much less spatially extended than in the prominent $z = 5.17$–5.20 overdensity that is the focus of this study.

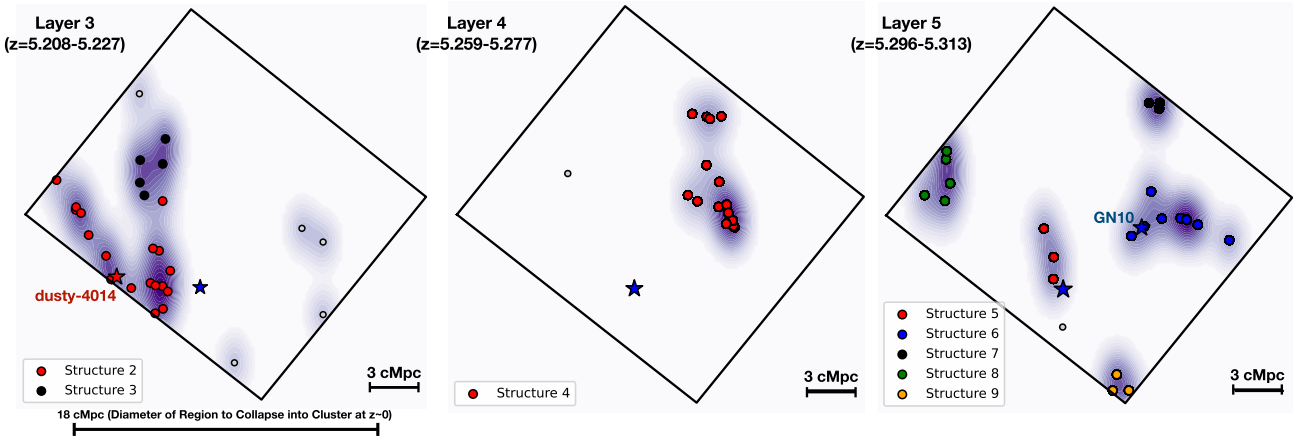

Figure A1. Similar to Fig. 7, but for the identified structures in the overdensities of star-forming galaxies we have identified over the GOODS North FRESCO field at $z \sim 5.22$, ~ 5.27, and ~ 5.30. The red and blue stars indicate the position of dusty-4014 (dust-obscured galaxy identified by Matthee et al. 2024; Xiao et al. 2024 showing Hα in emission) and GN10 (Daddi et al. 2009; Riechers et al. 2020), respectively. The spatial extent of the substructures range from 1 to 4 cMpc in size.

APPENDIX B: Hα EMITTERS IDENTIFIED IN THE z∼5.15–5.31 OVERDENSITY OVER THE GOODS NORTH FRESCO FIELD

In this appendix, we provide a full catalogue of the star-forming galaxies identified as part of the prominent $z = 5.15$–5.31 overdensity over the GOODS North FRESCO field. Coordinates for individual sources in the overdensity, together with their redshift determinations, flux measurements in the $F210M$ band, Hα fluxes, stellar masses, SFRs, UV-continuum slopes, and V-band dust attenuations are provided in Table B1–B5. Also indicated are whether sources were previously reported as part of the Walter et al. (2012), Arrabal Haro et al. (2018), Riechers et al. (2020), Calvi et al. (2021), or Matthee et al. (2024) studies. Given the $\Delta z \sim 0.07$ uncertainties in the photometric redshifts derived as part of Arrabal Haro et al. (2018), sources in Arrabal Haro et al. (2018) are considered to be likely members of the overdensity at $z \sim 5.2$ if their photometry redshifts are $z > 5.13$ and $z < 5.27$. A machine readable format of this table is available as Supporting Information.

Table B1. Catalogues of star-forming galaxies at $z \sim 5.15-5.32$ that are part of the overdensity in the FRESCO GOODS North field.

ID	RA	Dec.	$z_{\rm spec}$[a]	m_{210} [mag]	$f_{\rm H\alpha}$ [10^{-18}erg s^{-1} cm^{-2}]	log(M$_\star$)	β	A_V	SFR	Ref[b]
					Extended structure 1A					
2152	12:36:25.39	62:11:19.8	5.161	25.6	15.0 ± 0.3	$9.57^{+0.25}_{-0.49}$	$-1.27^{+0.15}_{-0.11}$	$0.53^{+0.14}_{-0.23}$	$31.5^{+45.1}_{-15.4}$	
2096	12:36:24.97	62:11:18.2	5.163	25.7	5.3 ± 0.4	$9.79^{+0.18}_{-0.27}$	$-1.52^{+0.23}_{-0.20}$	$0.50^{+0.23}_{-0.17}$	$37.5^{+72.0}_{-25.9}$	
2037	12:36:24.68	62:11:17.0	5.167	25.9	7.6 ± 0.3	$9.93^{+0.29}_{-0.31}$	$-0.39^{+0.37}_{-0.42}$	$0.46^{+0.12}_{-0.20}$	$27.5^{+48.1}_{-19.9}$	
dusty-1257[b]	12:36:24.68	62:11:17.0	5.167	25.9	7.6 ± 0.3	> 9.7[c]	–[c]	–[c]	–[c]	[6]
					Extended structure 1B					
10338	12:36:30.69	62:13:44.0	5.172	28.4	1.2 ± 0.1	$7.40^{+0.31}_{-0.13}$	$-2.38^{+0.18}_{-0.11}$	$0.90^{+0.04}_{-0.06}$	$0.5^{+0.5}_{-0.1}$	
10351	12:36:30.63	62:13:44.1	5.173	27.3	1.9 ± 0.2	$8.65^{+0.26}_{-0.23}$	$-2.02^{+0.10}_{-0.10}$	$0.69^{+0.14}_{-0.22}$	$7.0^{+5.2}_{-2.8}$	
9967	12:36:31.37	62:13:39.0	5.173	27.8	2.4 ± 0.2	$8.42^{+0.21}_{-0.68}$	$-2.15^{+0.12}_{-0.14}$	$0.61^{+0.24}_{-0.30}$	$3.0^{+5.9}_{-2.1}$	
9247	12:36:28.75	62:13:30.0	5.174	27.8	1.3 ± 0.2	$8.36^{+0.61}_{-0.23}$	$-2.20^{+0.08}_{-0.07}$	$0.84^{+0.12}_{-0.48}$	$3.5^{+6.1}_{-1.9}$	
8799	12:36:33.73	62:13:22.9	5.175	27.2	1.7 ± 0.2	$8.82^{+0.18}_{-0.30}$	$-2.02^{+0.12}_{-0.09}$	$0.56^{+0.26}_{-0.16}$	$8.2^{+9.3}_{-4.4}$	
9982	12:36:31.98	62:13:39.0	5.178	25.0	13.0 ± 0.4	$10.07^{+0.17}_{-0.53}$	$-1.52^{+0.12}_{-0.13}$	$0.57^{+0.26}_{-0.15}$	$38.4^{+31.6}_{-18.2}$	
8586	12:36:35.87	62:13:19.1	5.179	25.8	2.6 ± 0.4	$9.44^{+0.25}_{-0.63}$	$-2.14^{+0.10}_{-0.10}$	$0.70^{+0.14}_{-0.25}$	$19.7^{+34.3}_{-8.7}$	
9754	12:36:31.83	62:13:36.2	5.179	26.5	4.7 ± 0.2	$9.16^{+0.33}_{-0.32}$	$-2.02^{+0.10}_{-0.08}$	$0.35^{+0.28}_{-0.18}$	$27.9^{+30.8}_{-14.5}$	
10431	12:36:30.22	62:13:45.0	5.180	25.5	8.8 ± 0.3	$9.65^{+0.18}_{-0.38}$	$-1.69^{+0.09}_{-0.10}$	$0.56^{+0.15}_{-0.14}$	$39.0^{+37.9}_{-17.7}$	
10723	12:36:29.11	62:13:49.0	5.181	27.6	1.5 ± 0.2	$8.14^{+0.20}_{-0.21}$	$-2.46^{+0.09}_{-0.08}$	$0.95^{+0.03}_{-0.10}$	$2.5^{+1.3}_{-0.9}$	
9362	12:36:32.49	62:13:31.3	5.181	25.6	8.9 ± 0.3	$9.51^{+0.12}_{-0.26}$	$-2.15^{+0.09}_{-0.06}$	$0.47^{+0.19}_{-0.19}$	$60.6^{+33.6}_{-25.6}$	
8576	12:36:28.07	62:13:19.5	5.182	26.7	5.1 ± 0.2	$9.11^{+0.16}_{-0.13}$	$-1.89^{+0.10}_{-0.12}$	$0.51^{+0.16}_{-0.11}$	$21.3^{+11.2}_{-10.2}$	
					Extended structure 1C					
7709	12:36:59.75	62:13:06.1	5.173	27.0	2.9 ± 0.3	$8.87^{+0.20}_{-0.30}$	$-1.88^{+0.12}_{-0.12}$	$0.58^{+0.17}_{-0.11}$	$9.4^{+7.2}_{-4.4}$	
3946	12:36:57.24	62:12:00.8	5.177	26.7	2.0 ± 0.3	$8.93^{+0.55}_{-0.43}$	$-1.55^{+0.15}_{-0.12}$	$0.61^{+0.10}_{-0.09}$	$7.0^{+10.0}_{-3.6}$	
6654	12:36:57.28	62:12:49.3	5.178	26.5	2.0 ± 0.3	$8.87^{+0.31}_{-0.20}$	$-2.19^{+0.08}_{-0.07}$	$0.89^{+0.07}_{-0.14}$	$8.7^{+6.8}_{-3.3}$	[1]
S3	12:36:56.56	62:12:07.4	5.179	28.2	5.3 ± 0.3	> 9.7[c]	–[c]	–[c]	–[c]	[6]
4528	12:36:59.25	62:12:12.3	5.184	26.7	3.7 ± 0.3	$9.34^{+0.29}_{-0.52}$	$-1.16^{+0.16}_{-0.18}$	$0.57^{+0.14}_{-0.14}$	$11.4^{+11.9}_{-10.1}$	
					Extended structure 1D					
1586	12:36:42.60	62:11:04.4	5.177	25.8	3.6 ± 0.4	$9.47^{+0.25}_{-0.39}$	$-1.97^{+0.10}_{-0.08}$	$0.79^{+0.14}_{-0.33}$	$24.5^{+13.9}_{-13.5}$	
128	12:36:36.57	62:09:45.1	5.178	27.5	2.0 ± 0.2	$8.00^{+0.46}_{-0.41}$	$-2.27^{+0.10}_{-0.08}$	$0.93^{+0.04}_{-0.06}$	$1.5^{+1.7}_{-0.6}$	
391	12:36:44.76	62:10:08.8	5.178	–	2.2 ± 0.2	$8.67^{+0.24}_{-0.35}$	$-1.72^{+0.23}_{-0.18}$	$0.65^{+0.14}_{-0.17}$	$4.9^{+4.7}_{-2.8}$	
169	12:36:39.79	62:09:49.1	5.179	25.2	20.0 ± 0.3	$9.93^{+0.18}_{-0.61}$	$-1.60^{+0.14}_{-0.10}$	$0.53^{+0.18}_{-0.17}$	$36.2^{+57.1}_{-17.3}$	[2]
999	12:36:45.47	62:10:46.5	5.181	27.9	4.8 ± 0.2	$7.26^{+0.47}_{-0.12}$	$-2.22^{+0.11}_{-0.10}$	$0.87^{+0.05}_{-0.05}$	$0.4^{+0.5}_{-0.1}$	
1512	12:36:40.72	62:11:02.0	5.182	26.0	5.0 ± 0.4	$8.86^{+0.41}_{-0.26}$	$-2.24^{+0.06}_{-0.06}$	$0.95^{+0.03}_{-0.05}$	$12.2^{+6.1}_{-6.6}$	
1852	12:36:42.17	62:11:12.2	5.184	24.9	7.4 ± 0.6	$10.19^{+0.24}_{-0.48}$	$-1.70^{+0.10}_{-0.10}$	$0.56^{+0.21}_{-0.34}$	$86.9^{+307.9}_{-51.8}$	
					Extended structure 1E					
5286	12:36:50.32	62:12:26.1	5.180	26.4	5.0 ± 0.3	$8.78^{+0.20}_{-0.16}$	$-2.08^{+0.12}_{-0.08}$	$0.70^{+0.13}_{-0.13}$	$9.7^{+5.0}_{-2.9}$	
6557	12:36:49.86	62:12:47.7	5.180	25.8	7.9 ± 0.4	$9.69^{+0.23}_{-0.61}$	$-1.48^{+0.12}_{-0.11}$	$0.55^{+0.25}_{-0.17}$	$27.4^{+39.3}_{-15.4}$	
8406	12:36:46.07	62:13:16.9	5.180	27.2	1.7 ± 0.2	$8.37^{+0.19}_{-0.26}$	$-2.23^{+0.08}_{-0.07}$	$0.94^{+0.04}_{-0.09}$	$3.1^{+1.5}_{-1.5}$	[1]
7003	12:36:49.51	62:12:55.2	5.182	26.1	3.9 ± 0.2	$9.44^{+0.32}_{-0.50}$	$-1.88^{+0.14}_{-0.07}$	$0.59^{+0.15}_{-0.20}$	$17.9^{+15.0}_{-9.1}$	
7296	12:36:53.09	62:12:59.5	5.183	26.6	3.6 ± 0.4	$8.65^{+0.54}_{-0.34}$	$-1.89^{+0.08}_{-0.07}$	$0.79^{+0.13}_{-0.12}$	$4.9^{+5.2}_{-2.0}$	[1]
8178	12:36:56.51	62:13:13.5	5.184	26.8	4.3 ± 0.3	$8.75^{+0.20}_{-0.39}$	$-2.21^{+0.10}_{-0.11}$	$0.80^{+0.13}_{-0.32}$	$5.5^{+4.6}_{-3.0}$	[1,3]

Table B1 – *continued*

ID	RA	Dec.	z_{spec}[a]	m_{210} [mag]	$f_{H\alpha}$ [10^{-18}erg s^{-1} cm^{-2}]	log(M$_\star$)	β	A_V	SFR	Ref[b]
4783	12:36:48.71	62:12:16.8	5.185	24.1	38.0 ± 0.7	$10.40^{+0.12}_{-0.25}$	$-0.71^{+0.14}_{-0.09}$	$0.65^{+0.10}_{-0.14}$	$107.0^{+121.0}_{-43.4}$	
HDF850.1	12:36:51.97	62:12:26.0	5.188	24.0	$6.5.0 \pm 0.4$	$10.9^{+0.4}_{-0.3}$	–	–	–	[1,6]
					Extended structure 1F					
3678	12:36:25.72	62:11:55.1	5.179	27.6	1.8 ± 0.3	$8.33^{+0.25}_{-0.32}$	$-2.12^{+0.16}_{-0.13}$	$0.79^{+0.11}_{-0.17}$	$2.4^{+2.5}_{-1.3}$	
5143	12:36:23.18	62:12:23.3	5.179	27.6	3.5 ± 0.2	$8.15^{+0.33}_{-0.39}$	$-1.49^{+0.23}_{-0.17}$	$0.57^{+0.16}_{-0.10}$	$2.4^{+2.4}_{-1.4}$	
2087	12:36:23.22	62:11:18.3	5.181	26.1	6.1 ± 0.5	$9.32^{+0.59}_{-0.61}$	$-1.76^{+0.14}_{-0.14}$	$0.45^{+0.33}_{-0.26}$	$18.3^{+31.9}_{-10.4}$	
3888	12:36:20.13	62:11:58.6	5.183	25.2	24.0 ± 0.5	$9.72^{+0.30}_{-0.39}$	$-1.40^{+0.12}_{-0.09}$	$0.45^{+0.19}_{-0.12}$	$48.8^{+54.3}_{-20.3}$	
4251	12:36:18.77	62:12:06.3	5.183	27.9	1.5 ± 0.2	$8.45^{+0.20}_{-0.43}$	$-2.04^{+0.16}_{-0.13}$	$0.68^{+0.15}_{-0.13}$	$3.5^{+3.8}_{-1.8}$	
5146	12:36:23.28	62:12:23.0	5.187	26.3	6.7 ± 0.3	$9.30^{+0.20}_{-0.31}$	$-1.40^{+0.15}_{-0.19}$	$0.52^{+0.17}_{-0.14}$	$18.2^{+26.5}_{-10.1}$	
4919	12:36:17.66	62:12:19.3	5.188	27.8	1.7 ± 0.2	$8.46^{+0.26}_{-0.36}$	$-1.95^{+0.16}_{-0.23}$	$0.83^{+0.09}_{-0.13}$	$1.3^{+1.2}_{-0.6}$	
					Extended structure 1G					
26025	12:36:43.38	62:16:56.1	5.186	26.2	8.9 ± 0.3	$9.39^{+0.18}_{-0.20}$	$-1.65^{+0.11}_{-0.12}$	$0.45^{+0.13}_{-0.09}$	$31.4^{+14.8}_{-11.7}$	
24928	12:36:40.75	62:16:38.3	5.188	25.1	7.8 ± 0.4	$9.84^{+0.14}_{-0.12}$	$-1.20^{+0.11}_{-0.10}$	$0.80^{+0.05}_{-0.14}$	$38.5^{+24.1}_{-15.5}$	
24849	12:36:40.71	62:16:37.4	5.190	27.2	2.4 ± 0.2	$8.91^{+0.27}_{-0.41}$	$-1.51^{+0.12}_{-0.16}$	$0.66^{+0.18}_{-0.19}$	$6.1^{+4.9}_{-3.5}$	

Notes.[a]Typical 1σ spectroscopic redshift uncertainties are ± 0.001.
[b] 1 = Walter et al. (2012), 2 = Arrabal Haro et al. (2018), 3 = Riechers et al. (2020), 4 = Calvi et al. (2021), 5 = Matthee et al. (2024), and 6 = Xiao et al. (2024).
[c] Presented in Xiao et al. (2024).

Table B2. Catalogues of star-forming galaxies at $z \sim 5.15-5.32$ that are part of the overdensity in the FRESCO GOODS North field.

ID	RA	Dec.	z_{spec}	m_{210} [mag]	$f_{H\alpha}$ [10^{-18}erg s^{-1} cm^{-2}]	log(M$_\star$)	β	A_V	SFR	Ref[a]
					Extended structure 1H					
23929	12:37:15.63	62:16:23.5	5.184	25.7	5.6 ± 0.3	$9.59^{+0.24}_{-0.53}$	$-2.15^{+0.08}_{-0.06}$	$0.65^{+0.24}_{-0.35}$	$25.7^{+85.6}_{-9.9}$	[1,2,3]
17512	12:37:12.62	62:15:04.1	5.185	25.4	4.4 ± 0.3	$9.95^{+0.10}_{-0.15}$	$-1.60^{+0.09}_{-0.09}$	$0.72^{+0.14}_{-0.22}$	$17.9^{+30.8}_{-13.6}$	
20673	12:37:17.87	62:15:40.7	5.187	26.7	1.8 ± 0.2	$9.28^{+0.22}_{-0.26}$	$-1.96^{+0.08}_{-0.08}$	$0.50^{+0.22}_{-0.27}$	$16.9^{+34.9}_{-10.7}$	
22471	12:37:15.70	62:16:03.0	5.187	25.1	8.1 ± 0.4	$10.23^{+0.21}_{-0.58}$	$-0.84^{+0.12}_{-0.19}$	$0.52^{+0.14}_{-0.18}$	$35.9^{+62.3}_{-11.9}$	
19988	12:37:14.51	62:15:32.5	5.188	25.3	4.7 ± 0.3	$9.37^{+0.33}_{-0.32}$	$-2.24^{+0.08}_{-0.08}$	$0.94^{+0.04}_{-0.07}$	$26.3^{+17.5}_{-11.3}$	[1,3]
21948	12:37:21.03	62:15:56.6	5.188	28.3	1.0 ± 0.2	$8.04^{+0.18}_{-0.26}$	$-2.15^{+0.08}_{-0.10}$	$0.77^{+0.08}_{-0.17}$	$2.1^{+1.1}_{-0.8}$	
23257	12:37:22.39	62:16:11.3	5.188	26.1	5.1 ± 0.3	$9.25^{+0.18}_{-0.16}$	$-2.03^{+0.09}_{-0.09}$	$0.59^{+0.21}_{-0.20}$	$28.8^{+16.0}_{-14.3}$	
16991	12:37:13.69	62:14:59.1	5.189	26.6	4.5 ± 0.4	$8.76^{+0.32}_{-0.36}$	$-1.89^{+0.08}_{-0.10}$	$0.66^{+0.14}_{-0.14}$	$8.0^{+4.9}_{-3.5}$	
17347	12:37:13.70	62:15:02.5	5.189	28.1	2.2 ± 0.3	$8.26^{+0.38}_{-0.43}$	$-1.30^{+0.28}_{-0.27}$	$0.56^{+0.18}_{-0.15}$	$1.9^{+2.3}_{-0.9}$	
20278	12:37:15.33	62:15:35.5	5.189	25.9	6.8 ± 0.3	$9.86^{+0.15}_{-0.17}$	$-1.29^{+0.10}_{-0.13}$	$0.47^{+0.12}_{-0.13}$	$23.0^{+21.8}_{-12.5}$	
21183	12:37:20.93	62:15:47.2	5.189	27.0	2.7 ± 0.3	$8.37^{+0.50}_{-0.34}$	$-2.16^{+0.12}_{-0.10}$	$0.84^{+0.09}_{-0.10}$	$2.9^{+7.0}_{-1.3}$	
23256	12:37:22.28	62:16:13.2	5.191	25.2	5.6 ± 0.5	$9.74^{+0.41}_{-0.45}$	$-1.67^{+0.10}_{-0.12}$	$0.73^{+0.14}_{-0.27}$	$54.7^{+104.4}_{-24.1}$	
16264	12:37:14.53	62:14:51.5	5.192	26.1	8.2 ± 0.4	$9.59^{+0.16}_{-0.16}$	$-1.67^{+0.08}_{-0.10}$	$0.50^{+0.12}_{-0.12}$	$21.7^{+20.5}_{-10.2}$	
22058	12:37:20.97	62:15:58.0	5.192	27.1	4.1 ± 0.2	$8.72^{+0.26}_{-0.31}$	$-2.04^{+0.10}_{-0.09}$	$0.53^{+0.22}_{-0.16}$	$8.7^{+11.6}_{-4.5}$	
22414	12:37:18.99	62:16:02.7	5.193	26.9	3.4 ± 0.3	$8.65^{+0.38}_{-0.36}$	$-2.01^{+0.11}_{-0.10}$	$0.84^{+0.09}_{-0.09}$	$4.0^{+2.3}_{-2.1}$	
21405	12:37:15.69	62:15:49.8	5.194	26.2	14.0 ± 0.3	$9.39^{+0.17}_{-0.19}$	$-1.54^{+0.10}_{-0.11}$	$0.35^{+0.13}_{-0.11}$	$34.1^{+27.1}_{-15.4}$	
					Extended structure 1I					
dusty-7162	12:37:16.90	62:14:00.9	5.189	25.1	30.0 ± 0.6	> 9.8[c]	–[c]	–[c]	–[c]	[6]
11708	12:37:16.87	62:14:00.2	5.189	25.1	30.0 ± 0.6	$9.52^{+0.25}_{-0.24}$	$-1.38^{+0.11}_{-0.09}$	$0.51^{+0.13}_{-0.12}$	$65.1^{+44.1}_{-21.4}$	
8937	12:37:17.34	62:13:25.2	5.191	25.8	7.3 ± 0.3	$9.32^{+0.21}_{-0.44}$	$-2.04^{+0.09}_{-0.07}$	$0.77^{+0.11}_{-0.22}$	$15.1^{+16.3}_{-7.2}$	[1]
8947	12:37:17.16	62:13:25.4	5.196	27.8	1.1 ± 0.1	$8.83^{+0.35}_{-0.26}$	$-1.61^{+0.18}_{-0.17}$	$0.55^{+0.26}_{-0.29}$	$7.2^{+12.0}_{-5.2}$	
					Extended structure 1J					
20034	12:36:55.50	62:15:32.8	5.187	26.5	10.0 ± 0.2	$8.27^{+0.52}_{-0.20}$	$-2.06^{+0.06}_{-0.13}$	$0.80^{+0.07}_{-0.08}$	$4.1^{+6.8}_{-1.7}$	[1,2]
19533	12:36:56.35	62:15:27.0	5.188	25.3	13.0 ± 0.3	$9.76^{+0.19}_{-0.31}$	$-1.49^{+0.08}_{-0.11}$	$0.46^{+0.17}_{-0.19}$	$85.4^{+86.1}_{-51.9}$	
21166	12:36:52.21	62:15:47.2	5.188	27.4	1.5 ± 0.2	$8.52^{+0.18}_{-0.19}$	$-2.24^{+0.09}_{-0.09}$	$0.87^{+0.07}_{-0.26}$	$4.5^{+3.5}_{-2.2}$	
22601	12:36:52.34	62:16:05.1	5.189	25.3	8.1 ± 0.5	$9.38^{+0.50}_{-0.26}$	$-1.86^{+0.09}_{-0.10}$	$0.72^{+0.14}_{-0.26}$	$31.4^{+32.7}_{-15.7}$	
20499	12:36:49.23	62:15:38.6	5.190	25.1	18.0 ± 0.4	$9.19^{+0.22}_{-0.27}$	$-2.33^{+0.06}_{-0.05}$	$0.88^{+0.07}_{-0.20}$	$22.1^{+18.8}_{-11.7}$	[1,2]

Table B2 – *continued*

ID	RA	Dec.	z_{spec}	m_{210} [mag]	$f_{H\alpha}$ [10^{-18}erg s^{-1} cm^{-2}]	log(M$_\star$)	β	A_V	SFR	Ref[a]
21309	12:36:55.39	62:15:48.8	5.191	26.8	3.6 ± 0.2	$8.71^{+0.28}_{-0.46}$	$-2.17^{+0.08}_{-0.08}$	$0.60^{+0.23}_{-0.15}$	$9.6^{+7.5}_{-5.6}$	[1,2]
23345	12:36:58.43	62:16:15.0	5.192	26.2	3.5 ± 0.3	$8.96^{+0.44}_{-0.26}$	$-2.11^{+0.06}_{-0.07}$	$0.80^{+0.10}_{-0.34}$	$13.1^{+14.7}_{-5.7}$	[1,3]
24252	12:36:57.30	62:16:28.6	5.192	27.2	1.5 ± 0.2	$8.21^{+0.23}_{-0.36}$	$-2.31^{+0.04}_{-0.05}$	$0.97^{+0.01}_{-0.03}$	$3.2^{+2.0}_{-1.6}$	
24125	12:36:57.36	62:16:26.6	5.193	27.6	1.9 ± 0.2	$8.76^{+0.21}_{-0.26}$	$-1.91^{+0.09}_{-0.10}$	$0.68^{+0.14}_{-0.23}$	$2.8^{+4.5}_{-1.4}$	
26715	12:36:56.62	62:17:08.0	5.194	28.2	2.9 ± 0.2	$9.09^{+0.20}_{-0.13}$	$-1.88^{+0.09}_{-0.08}$	$0.14^{+0.06}_{-0.04}$	$24.1^{+9.5}_{-7.8}$	
dusty-16116	12:36:56.62	62:17:08.0	5.194	28.2	2.9 ± 0.2	$9.09^{+0.20}_{-0.13}$	$-1.88^{+0.09}_{-0.08}$	$0.14^{+0.06}_{-0.04}$	$24.1^{+9.5}_{-7.8}$	[6]
28034	12:36:52.80	62:17:36.2	5.196	28.1	0.7 ± 0.1	$8.07^{+0.30}_{-0.19}$	$-2.35^{+0.13}_{-0.08}$	$0.86^{+0.10}_{-0.16}$	$2.4^{+1.7}_{-0.9}$	
					Extended structure 1K					
24946	12:37:11.11	62:16:38.6	5.193	25.3	15.0 ± 0.4	$9.88^{+0.15}_{-0.34}$	$-1.47^{+0.09}_{-0.09}$	$0.48^{+0.17}_{-0.11}$	$49.3^{+34.8}_{-25.5}$	[1,2]
25788	12:37:16.07	62:16:51.7	5.194	25.3	17.0 ± 0.4	$9.50^{+0.31}_{-0.23}$	$-1.92^{+0.14}_{-0.08}$	$0.46^{+0.09}_{-0.14}$	$71.6^{+51.7}_{-30.7}$	
24574	12:37:13.73	62:16:33.2	5.195	28.1	3.1 ± 0.3	$7.96^{+0.54}_{-0.17}$	$-1.75^{+0.15}_{-0.16}$	$0.74^{+0.07}_{-0.10}$	$1.6^{+3.0}_{-0.9}$	
					Extended structure 1L					
22502	12:37:05.58	62:16:03.9	5.193	25.5	8.7 ± 0.5	$9.58^{+0.25}_{-0.29}$	$-1.95^{+0.12}_{-0.08}$	$0.51^{+0.17}_{-0.18}$	$44.0^{+43.6}_{-18.3}$	
22858	12:37:06.63	62:16:08.7	5.194	27.2	3.5 ± 0.3	$8.70^{+0.23}_{-0.33}$	$-1.50^{+0.17}_{-0.15}$	$0.64^{+0.09}_{-0.07}$	$5.3^{+4.5}_{-2.7}$	
22295	12:37:05.52	62:16:01.3	5.195	27.4	3.6 ± 0.3	$7.73^{+0.64}_{-0.23}$	$-2.33^{+0.15}_{-0.11}$	$0.94^{+0.04}_{-0.05}$	$0.8^{+0.5}_{-0.2}$	[1,3]
22826	12:37:03.90	62:16:08.4	5.195	27.6	1.3 ± 0.2	$8.61^{+0.30}_{-0.30}$	$-2.14^{+0.09}_{-0.08}$	$0.82^{+0.13}_{-0.13}$	$4.9^{+4.3}_{-1.9}$	
					Extended structure 1M					
29679	12:36:39.72	62:18:24.8	5.192	25.7	4.4 ± 0.3	$9.58^{+0.28}_{-0.28}$	$-1.99^{+0.07}_{-0.09}$	$0.57^{+0.33}_{-0.34}$	$39.5^{+88.1}_{-26.2}$	
29651	12:36:39.67	62:18:23.8	5.194	27.6	1.1 ± 0.1	$8.32^{+0.23}_{-0.17}$	$-2.11^{+0.14}_{-0.15}$	$0.76^{+0.10}_{-0.17}$	$4.6^{+2.6}_{-1.5}$	
29544	12:36:39.98	62:18:20.2	5.195	25.5	10.0 ± 0.3	$9.97^{+0.38}_{-0.39}$	$-1.24^{+0.12}_{-0.12}$	$0.43^{+0.24}_{-0.17}$	$60.1^{+109.7}_{-35.6}$	
					Extended structure 1 – General					
13227	12:36:58.22	62:14:18.7	5.151	27.7	1.2 ± 0.2	$8.51^{+0.25}_{-0.30}$	$-1.92^{+0.16}_{-0.15}$	$0.73^{+0.16}_{-0.28}$	$4.7^{+4.9}_{-2.5}$	
4303	12:36:56.52	62:12:07.6	5.164	28.2	5.3 ± 0.3	$9.30^{+0.35}_{-0.31}$	$2.91^{+2.90}_{-2.50}$	$0.15^{+0.10}_{-0.09}$	$14.9^{+17.4}_{-9.9}$	
23280	12:37:22.17	62:16:14.0	5.165	26.9	4.1 ± 0.3	$8.51^{+0.31}_{-0.41}$	$-1.57^{+0.20}_{-0.27}$	$0.60^{+0.18}_{-0.14}$	$4.9^{+3.6}_{-2.5}$	
8619	12:36:27.98	62:13:19.9	5.165	28.3	1.4 ± 0.2	$8.40^{+0.38}_{-0.31}$	$-1.96^{+0.27}_{-0.17}$	$0.81^{+0.14}_{-0.26}$	$2.0^{+2.9}_{-1.4}$	
4796	12:36:20.66	62:12:16.8	5.166	26.9	2.7 ± 0.2	$8.85^{+0.18}_{-0.35}$	$-1.85^{+0.19}_{-0.09}$	$0.71^{+0.13}_{-0.25}$	$5.8^{+6.2}_{-3.8}$	

Notes. [a]1 = Walter et al. (2012), 2 = Arrabal Haro et al. (2018), 3 = Riechers et al. (2020), 4 = Calvi et al. (2021), 5 = Matthee et al. (2024), and 6 = Xiao et al. (2024).
[c]Presented in Xiao et al. (2024).

Table B3. Catalogues of star-forming galaxies at $z \sim 5.15-5.32$ that are part of the overdensity in the FRESCO GOODS North field.

ID	RA	Dec.	z_{spec}	m_{210} [mag]	$f_{H\alpha}$ [10^{-18}erg s^{-1} cm^{-2}]	log(M$_\star$)	β	A_V	SFR	Ref[a]
					Extended structure 1 – General					
5578	12:37:06.17	62:12:30.7	5.172	27.8	1.3 ± 0.2	$8.43^{+0.19}_{-0.24}$	$-2.06^{+0.14}_{-0.12}$	$0.74^{+0.16}_{-0.28}$	$4.2^{+3.1}_{-1.7}$	
16542	12:36:59.68	62:14:54.4	5.178	25.3	12.0 ± 0.5	$10.01^{+0.11}_{-0.12}$	$-1.02^{+0.11}_{-0.13}$	$0.66^{+0.09}_{-0.14}$	$49.7^{+54.6}_{-31.0}$	
17877	12:37:08.08	62:15:08.2	5.178	28.0	1.9 ± 0.2	$8.56^{+0.48}_{-0.30}$	$-2.02^{+0.12}_{-0.12}$	$0.69^{+0.15}_{-0.41}$	$3.4^{+8.5}_{-2.0}$	
5848	12:36:37.52	62:12:36.0	5.179	26.1	5.5 ± 0.3	$9.41^{+0.27}_{-0.15}$	$-1.69^{+0.08}_{-0.09}$	$0.53^{+0.26}_{-0.18}$	$27.3^{+24.4}_{-23.6}$	[1,2]
10187	12:37:12.39	62:13:42.1	5.181	27.3	1.5 ± 0.3	$8.31^{+0.38}_{-0.64}$	$-2.13^{+0.12}_{-0.13}$	$0.88^{+0.07}_{-0.13}$	$1.6^{+2.0}_{-0.7}$	
10218	12:37:05.64	62:13:42.1	5.181	26.3	3.4 ± 0.4	$8.96^{+0.37}_{-0.26}$	$-2.21^{+0.06}_{-0.06}$	$0.90^{+0.07}_{-0.17}$	$8.5^{+4.6}_{-2.2}$	
15198	12:36:28.23	62:14:39.6	5.181	27.0	2.6 ± 0.2	$8.96^{+0.17}_{-0.49}$	$-2.05^{+0.08}_{-0.09}$	$0.64^{+0.20}_{-0.22}$	$10.1^{+14.4}_{-6.0}$	
14125	12:36:50.06	62:14:28.7	5.182	27.5	1.5 ± 0.2	$8.48^{+0.17}_{-0.19}$	$-2.04^{+0.09}_{-0.12}$	$0.74^{+0.12}_{-0.14}$	$5.1^{+2.8}_{-2.2}$	
1820	12:36:51.79	62:11:11.3	5.182	26.0	12.0 ± 0.3	$9.64^{+0.24}_{-0.28}$	$-1.56^{+0.11}_{-0.10}$	$0.53^{+0.13}_{-0.20}$	$19.6^{+22.3}_{-10.1}$	
3176	12:36:52.03	62:11:44.9	5.182	25.7	8.7 ± 0.5	$9.20^{+0.41}_{-0.28}$	$-1.56^{+0.14}_{-0.12}$	$0.65^{+0.16}_{-0.13}$	$21.1^{+14.6}_{-11.8}$	
5587	12:36:29.12	62:12:30.7	5.182	27.1	5.2 ± 0.3	$8.62^{+0.26}_{-0.35}$	$-1.84^{+0.21}_{-0.16}$	$0.59^{+0.12}_{-0.21}$	$4.7^{+5.9}_{-2.4}$	
19527	12:36:38.42	62:15:27.2	5.189	25.7	5.1 ± 0.4	$9.78^{+0.12}_{-0.07}$	$-1.17^{+0.10}_{-0.15}$	$0.72^{+0.09}_{-0.26}$	$31.0^{+41.6}_{-16.2}$	[1]

Table B3 – *continued*

ID	RA	Dec.	$z_{\rm spec}$	m_{210} [mag]	$f_{\rm H\alpha}$ [10^{-18}erg s^{-1} cm^{-2}]	log(M$_\star$)	β	A_V	SFR	Ref[a]
26502	12:36:47.26	62:17:04.2	5.191	26.0	2.6 ± 0.2	$9.55^{+0.28}_{-0.27}$	$-2.14^{+0.06}_{-0.07}$	$0.65^{+0.22}_{-0.40}$	$30.5^{+62.4}_{-17.9}$	
29562	12:36:52.33	62:18:20.9	5.191	27.8	1.4 ± 0.2	$8.26^{+0.31}_{-0.23}$	$-2.27^{+0.10}_{-0.07}$	$0.91^{+0.07}_{-0.12}$	$2.0^{+2.5}_{-1.2}$	
4306	12:36:26.48	62:12:07.4	5.193	26.1	5.1 ± 0.3	$9.55^{+0.20}_{-0.25}$	$-1.67^{+0.11}_{-0.10}$	$0.52^{+0.16}_{-0.25}$	$29.9^{+43.0}_{-17.8}$	[1,2]
10911	12:36:24.08	62:13:51.2	5.197	26.3	3.6 ± 0.3	$9.40^{+0.12}_{-0.29}$	$-1.96^{+0.07}_{-0.04}$	$0.64^{+0.09}_{-0.27}$	$14.1^{+13.5}_{-5.6}$	[1]
16423	12:37:03.28	62:14:53.4	5.200	27.6	3.0 ± 0.2	$8.15^{+0.29}_{-0.32}$	$-1.83^{+0.13}_{-0.14}$	$0.63^{+0.11}_{-0.12}$	$2.5^{+2.1}_{-1.1}$	
					Extended structure 2					
9073	12:37:01.85	62:13:27.6	5.202	26.6	2.8 ± 0.4	$9.13^{+0.38}_{-0.39}$	$-1.76^{+0.12}_{-0.13}$	$0.65^{+0.18}_{-0.09}$	$11.0^{+9.6}_{-6.6}$	
6921	12:36:59.18	62:12:53.7	5.208	24.9	13.0 ± 0.3	$9.89^{+0.26}_{-0.52}$	$-1.22^{+0.09}_{-0.08}$	$0.54^{+0.26}_{-0.13}$	$60.7^{+66.4}_{-24.4}$	
16253	12:37:01.00	62:14:51.6	5.209	28.2	1.1 ± 0.2	$7.99^{+0.34}_{-0.49}$	$-1.74^{+0.20}_{-0.18}$	$0.75^{+0.10}_{-0.20}$	$1.4^{+2.1}_{-0.7}$	
9370	12:37:03.31	62:13:31.4	5.212	25.7	20.0 ± 0.4	$9.48^{+0.14}_{-0.22}$	$-1.94^{+0.08}_{-0.07}$	$0.42^{+0.10}_{-0.09}$	$57.6^{+32.5}_{-23.8}$	[1,3]
3374	12:37:00.92	62:11:49.3	5.219	26.9	4.9 ± 0.2	$8.80^{+0.30}_{-0.46}$	$-1.17^{+0.20}_{-0.18}$	$0.53^{+0.14}_{-0.12}$	$8.6^{+8.9}_{-4.5}$	
5204	12:37:08.53	62:12:24.5	5.219	25.5	5.7 ± 0.2	$9.87^{+0.35}_{-0.27}$	$-1.89^{+0.11}_{-0.08}$	$0.59^{+0.21}_{-0.47}$	$57.5^{+329.2}_{-36.8}$	
3023	12:37:02.80	62:11:41.7	5.220	–	4.3 ± 0.2	$9.24^{+0.33}_{-0.33}$	$-1.79^{+0.17}_{-0.13}$	$0.58^{+0.18}_{-0.20}$	$18.2^{+19.1}_{-12.1}$	
6061	12:37:13.38	62:12:39.1	5.220	–	11.0 ± 0.3	$9.51^{+0.10}_{-0.26}$	$-2.14^{+0.09}_{-0.09}$	$0.64^{+0.19}_{-0.22}$	$57.9^{+24.0}_{-27.2}$	[1]
5396	12:37:01.03	62:12:27.7	5.221	26.6	3.7 ± 0.2	$9.05^{+0.22}_{-0.21}$	$-1.73^{+0.10}_{-0.10}$	$0.56^{+0.18}_{-0.23}$	$17.0^{+13.4}_{-10.6}$	
dusty-4014	12:37:12.03	62:12:43.4	5.221	–	–	$> 9.8^{c}$	–[c]	–[c]	–[c]	[5,6]
11160	12:37:18.76	62:13:54.1	5.222	27.9	1.7 ± 0.2	$8.85^{+0.27}_{-0.41}$	$-1.76^{+0.15}_{-0.16}$	$0.71^{+0.15}_{-0.33}$	$4.8^{+8.2}_{-2.7}$	
14954	12:37:21.87	62:14:36.9	5.222	27.4	2.0 ± 0.3	$8.40^{+0.38}_{-0.52}$	$-2.18^{+0.13}_{-0.12}$	$0.92^{+0.05}_{-0.05}$	$2.6^{+1.4}_{-1.1}$	
19541	12:37:26.47	62:15:27.1	5.222	26.5	4.6 ± 0.3	$8.91^{+0.24}_{-0.24}$	$-2.10^{+0.08}_{-0.09}$	$0.62^{+0.16}_{-0.21}$	$14.1^{+9.2}_{-5.2}$	
4927	12:36:59.79	62:12:18.7	5.222	23.9	35.0 ± 0.7	$10.42^{+0.19}_{-0.30}$	$-1.69^{+0.16}_{-0.09}$	$0.62^{+0.13}_{-0.15}$	$103.7^{+190.0}_{-64.1}$	
5702	12:37:03.94	62:12:32.9	5.223	25.2	8.2 ± 0.3	$9.95^{+0.12}_{-0.27}$	$-2.01^{+0.06}_{-0.04}$	$0.61^{+0.14}_{-0.22}$	$56.7^{+71.5}_{-25.0}$	
8544	12:37:14.58	62:13:18.9	5.223	26.1	4.8 ± 0.2	$9.41^{+0.34}_{-0.21}$	$-1.44^{+0.13}_{-0.11}$	$0.51^{+0.15}_{-0.12}$	$43.3^{+26.2}_{-22.3}$	
14421	12:37:20.58	62:14:31.3	5.225	26.6	5.1 ± 0.3	$8.77^{+0.25}_{-0.25}$	$-1.77^{+0.18}_{-0.13}$	$0.60^{+0.16}_{-0.10}$	$9.5^{+6.4}_{-4.9}$	
15403	12:37:21.78	62:14:41.4	5.225	26.9	4.8 ± 0.3	$8.65^{+0.20}_{-0.22}$	$-2.02^{+0.08}_{-0.10}$	$0.60^{+0.15}_{-0.11}$	$8.6^{+4.8}_{-3.3}$	
5467	12:37:02.73	62:12:28.8	5.227	25.4	19.0 ± 0.4	$9.68^{+0.15}_{-0.25}$	$-1.55^{+0.09}_{-0.09}$	$0.53^{+0.11}_{-0.15}$	$55.4^{+53.2}_{-16.0}$	[1]
					Extended structure 3					
21767	12:37:00.98	62:15:54.5	5.224	28.8	1.1 ± 0.1	$7.80^{+0.60}_{-0.70}$	$-1.91^{+0.21}_{-0.29}$	$0.74^{+0.16}_{-0.27}$	$0.4^{+1.6}_{-0.2}$	
24801	12:37:00.32	62:16:36.7	5.224	27.6	1.3 ± 0.2	$8.65^{+0.19}_{-0.37}$	$-2.10^{+0.08}_{-0.11}$	$0.72^{+0.19}_{-0.31}$	$4.7^{+5.6}_{-2.4}$	
22259	12:37:06.39	62:16:00.9	5.227	27.9	2.0 ± 0.3	$8.24^{+0.42}_{-0.33}$	$-2.14^{+0.13}_{-0.12}$	$0.79^{+0.12}_{-0.33}$	$2.5^{+2.7}_{-1.5}$	
17190	12:37:05.38	62:15:01.3	5.234	27.3	1.7 ± 0.2	$8.79^{+0.25}_{-0.45}$	$-2.10^{+0.09}_{-0.09}$	$0.84^{+0.10}_{-0.47}$	$4.1^{+6.6}_{-1.4}$	
19141	12:37:06.47	62:15:22.8	5.234	25.6	4.9 ± 0.4	$9.21^{+0.25}_{-0.18}$	$-2.26^{+0.08}_{-0.06}$	$0.82^{+0.13}_{-0.25}$	$24.6^{+29.6}_{-8.7}$	
					Extended structure 4					
15414	12:36:32.08	62:14:42.0	5.259	27.5	1.7 ± 0.2	$8.72^{+0.30}_{-0.38}$	$-1.80^{+0.17}_{-0.13}$	$0.57^{+0.19}_{-0.17}$	$7.3^{+6.3}_{-4.1}$	
26892	12:36:34.87	62:17:11.7	5.259	27.2	1.1 ± 0.2	$8.63^{+0.23}_{-0.27}$	$-2.13^{+0.10}_{-0.10}$	$0.79^{+0.17}_{-0.24}$	$3.9^{+6.0}_{-2.7}$	
15714	12:36:30.19	62:14:45.1	5.260	27.0	1.9 ± 0.2	$9.13^{+0.15}_{-0.28}$	$-1.76^{+0.17}_{-0.15}$	$0.48^{+0.25}_{-0.20}$	$10.6^{+16.7}_{-7.4}$	
21513	12:36:34.97	62:15:51.4	5.267	26.1	3.8 ± 0.2	$9.00^{+0.59}_{-0.24}$	$-1.85^{+0.09}_{-0.08}$	$0.74^{+0.11}_{-0.20}$	$12.6^{+15.2}_{-5.0}$	
26742	12:36:34.19	62:17:08.6	5.267	26.3	9.6 ± 0.3	$8.63^{+0.25}_{-0.42}$	$-2.23^{+0.11}_{-0.10}$	$0.86^{+0.05}_{-0.08}$	$4.6^{+3.4}_{-1.7}$	[1]
19203	12:36:31.94	62:15:23.6	5.268	27.8	2.7 ± 0.2	$8.21^{+0.23}_{-0.27}$	$-2.22^{+0.08}_{-0.09}$	$0.82^{+0.09}_{-0.11}$	$2.1^{+1.4}_{-1.0}$	
12288	12:36:28.30	62:14:07.9	5.269	27.8	2.0 ± 0.1	$8.24^{+0.14}_{-0.28}$	$-2.30^{+0.11}_{-0.11}$	$0.83^{+0.09}_{-0.22}$	$2.6^{+2.0}_{-1.4}$	
12805	12:36:30.28	62:14:13.8	5.269	26.7	2.7 ± 0.3	$8.64^{+0.33}_{-0.35}$	$-2.09^{+0.07}_{-0.08}$	$0.76^{+0.10}_{-0.17}$	$7.2^{+5.9}_{-4.1}$	
15715	12:36:30.18	62:14:45.4	5.269	27.0	2.1 ± 0.2	$8.59^{+0.19}_{-0.19}$	$-2.08^{+0.11}_{-0.10}$	$0.68^{+0.12}_{-0.21}$	$7.5^{+4.1}_{-2.9}$	
17226	12:36:39.34	62:15:01.6	5.269	27.2	3.0 ± 0.2	$8.07^{+0.32}_{-0.30}$	$-1.99^{+0.09}_{-0.10}$	$0.82^{+0.07}_{-0.10}$	$1.7^{+1.0}_{-0.6}$	
26941	12:36:31.44	62:17:12.6	5.269	26.2	4.2 ± 0.3	$9.53^{+0.16}_{-0.91}$	$-1.09^{+0.19}_{-0.11}$	$0.63^{+0.16}_{-0.23}$	$12.7^{+33.1}_{-4.7}$	
12538	12:36:28.58	62:14:10.5	5.271	25.9	7.6 ± 0.3	$9.33^{+0.21}_{-0.22}$	$-2.18^{+0.08}_{-0.08}$	$0.43^{+0.24}_{-0.15}$	$39.2^{+28.7}_{-19.1}$	
14448	12:36:29.80	62:14:32.0	5.271	26.8	3.8 ± 0.2	$9.04^{+0.18}_{-0.74}$	$-2.01^{+0.10}_{-0.11}$	$0.60^{+0.23}_{-0.25}$	$8.7^{+12.3}_{-5.3}$	

Notes. [a]1 = Walter et al. (2012), 2 = Arrabal Haro et al. (2018), 3 = Riechers et al. (2020), 4 = Calvi et al. (2021), 5 = Matthee et al. (2024), and 6 = Xiao et al. (2024).
[c]Presented in Xiao et al. (2024).

Table B4. Cataloguesof star-forming galaxies at $z \sim 5.15-5.32$ that are part of the overdensity in the FRESCO GOODS North field.

ID	RA	Dec.	z_{spec}	m_{210} [mag]	$f_{H\alpha}$ [10^{-18}erg s^{-1} cm^{-2}]	log(M$_\star$)	β	A_V	SFR	Ref[a]
					Extended structure 4					
13292	12:36:28.81	62:14:19.2	5.273	26.2	7.7 ± 0.3	$9.12^{+0.23}_{-0.20}$	$-2.05^{+0.08}_{-0.07}$	$0.38^{+0.21}_{-0.13}$	$24.3^{+18.6}_{-10.9}$	
13254	12:36:28.71	62:14:18.8	5.275	25.9	5.3 ± 0.4	$9.28^{+0.19}_{-0.20}$	$-2.08^{+0.07}_{-0.06}$	$0.53^{+0.23}_{-0.14}$	$29.9^{+15.8}_{-12.7}$	
16223	12:36:37.10	62:14:51.1	5.276	26.5	4.2 ± 0.3	$9.41^{+0.24}_{-0.27}$	$-1.83^{+0.10}_{-0.09}$	$0.53^{+0.31}_{-0.21}$	$11.5^{+14.7}_{-7.5}$	
27133	12:36:38.35	62:17:16.7	5.277	26.9	2.2 ± 0.3	$8.59^{+0.18}_{-0.24}$	$-2.06^{+0.10}_{-0.12}$	$0.85^{+0.07}_{-0.10}$	$7.4^{+3.6}_{-2.8}$	
					Extended structure 5					
12210	12:36:56.60	62:14:07.1	5.284	27.2	2.9 ± 0.2	$7.65^{+1.00}_{-0.39}$	$-2.43^{+0.13}_{-0.09}$	$0.95^{+0.04}_{-0.05}$	$0.4^{+0.3}_{-0.1}$	
8583	12:36:54.23	62:13:19.6	5.295	26.6	2.2 ± 0.2	$9.21^{+0.26}_{-0.50}$	$-2.06^{+0.06}_{-0.08}$	$0.68^{+0.15}_{-0.43}$	$12.1^{+24.2}_{-5.0}$	
6255	12:36:54.32	62:12:42.9	5.307	25.7	6.0 ± 0.4	$9.77^{+0.16}_{-0.16}$	$-1.49^{+0.11}_{-0.07}$	$0.61^{+0.18}_{-0.23}$	$31.5^{+42.2}_{-17.1}$	
					Extended structure 6					
11214	12:36:35.85	62:13:54.7	5.296	26.0	7.2 ± 0.2	$9.41^{+0.21}_{-0.25}$	$-1.78^{+0.09}_{-0.09}$	$0.63^{+0.14}_{-0.11}$	$14.7^{+11.7}_{-4.7}$	
13539	12:36:22.73	62:14:21.7	5.296	26.4	7.3 ± 0.3	$9.58^{+0.14}_{-0.23}$	$-1.67^{+0.08}_{-0.10}$	$0.37^{+0.22}_{-0.09}$	$26.6^{+26.2}_{-12.5}$	
10647	12:36:12.62	62:13:47.6	5.297	26.4	2.4 ± 0.1	$9.34^{+0.29}_{-0.30}$	$-1.78^{+0.11}_{-0.12}$	$0.49^{+0.31}_{-0.20}$	$23.4^{+25.8}_{-13.0}$	
13540	12:36:22.78	62:14:22.1	5.297	26.1	6.0 ± 0.3	$9.45^{+0.12}_{-0.57}$	$-2.03^{+0.16}_{-0.07}$	$0.75^{+0.12}_{-0.19}$	$14.2^{+18.0}_{-7.0}$	
13668	12:36:28.66	62:14:23.8	5.298	25.4	6.3 ± 0.3	$9.86^{+0.14}_{-0.35}$	$-1.54^{+0.08}_{-0.11}$	$0.58^{+0.22}_{-0.24}$	$63.8^{+86.5}_{-47.7}$	
12799	12:36:20.13	62:14:13.7	5.300	26.9	4.6 ± 0.2	$8.81^{+0.23}_{-0.37}$	$-2.09^{+0.10}_{-0.09}$	$0.68^{+0.11}_{-0.11}$	$5.8^{+6.5}_{-2.6}$	
17951	12:36:31.18	62:15:09.0	5.300	26.2	4.9 ± 0.2	$8.87^{+0.22}_{-0.24}$	$-2.18^{+0.07}_{-0.08}$	$0.73^{+0.13}_{-0.27}$	$13.3^{+9.0}_{-5.9}$	
12566	12:36:32.81	62:14:10.7	5.303	25.4	12.0 ± 0.3	$9.69^{+0.26}_{-0.34}$	$-0.94^{+0.11}_{-0.08}$	$0.67^{+0.10}_{-0.13}$	$29.0^{+30.5}_{-12.5}$	
13750	12:36:24.20	62:14:24.7	5.305	26.8	1.6 ± 0.2	$9.09^{+0.27}_{-0.31}$	$-2.00^{+0.14}_{-0.06}$	$0.76^{+0.15}_{-0.25}$	$7.7^{+8.7}_{-4.1}$	
GN10	12:36:33.42	62:14:08.6	5.306	–	–	$> 9.7^{c}$	$-^{c}$	$-^{c}$	$-^{c}$	[3,6]
					Extended structure 7					
27663	12:36:29.26	62:17:27.6	5.300	26.8	2.2 ± 0.2	$9.24^{+0.30}_{-0.40}$	$-1.67^{+0.13}_{-0.14}$	$0.59^{+0.13}_{-0.26}$	$12.1^{+28.2}_{-7.1}$	
28064	12:36:29.10	62:17:36.9	5.300	29.6	2.2 ± 0.1	$8.01^{+0.45}_{-0.46}$	$-1.80^{+0.21}_{-0.17}$	$0.68^{+0.12}_{-0.16}$	$1.1^{+2.3}_{-0.7}$	
28057	12:36:31.65	62:17:36.8	5.303	27.2	1.4 ± 0.1	$8.42^{+0.15}_{-0.25}$	$-1.82^{+0.10}_{-0.15}$	$0.80^{+0.08}_{-0.18}$	$5.2^{+2.3}_{-2.2}$	
					Extended structure 8					
22442	12:37:19.75	62:16:02.8	5.297	26.4	2.6 ± 0.2	$9.46^{+0.26}_{-0.42}$	$-1.89^{+0.10}_{-0.06}$	$0.58^{+0.22}_{-0.22}$	$22.3^{+14.8}_{-10.2}$	
23444	12:37:19.58	62:16:16.2	5.299	26.7	5.0 ± 0.2	$9.05^{+0.19}_{-0.21}$	$-1.10^{+0.14}_{-0.14}$	$0.54^{+0.11}_{-0.15}$	$19.6^{+11.4}_{-8.2}$	
19151	12:37:18.77	62:15:22.7	5.305	24.5	17.0 ± 0.5	$10.00^{+0.35}_{-0.26}$	$-1.43^{+0.08}_{-0.15}$	$0.69^{+0.08}_{-0.12}$	$100.5^{+100.2}_{-53.4}$	
16469	12:37:20.03	62:14:53.3	5.308	26.2	6.0 ± 0.4	$9.59^{+0.28}_{-0.54}$	$-1.05^{+0.15}_{-0.26}$	$0.66^{+0.14}_{-0.17}$	$11.1^{+12.4}_{-5.5}$	
17397	12:37:24.83	62:15:02.7	5.310	24.7	42.0 ± 0.6	$9.82^{+0.20}_{-0.18}$	$-1.35^{+0.10}_{-0.11}$	$0.44^{+0.11}_{-0.09}$	$113.8^{+60.3}_{-35.8}$	
					Extended structure 9					
315	12:36:39.31	62:10:03.4	5.302	26.0	6.2 ± 0.2	$9.10^{+0.22}_{-0.51}$	$-1.70^{+0.12}_{-0.15}$	$0.66^{+0.12}_{-0.21}$	$20.6^{+13.6}_{-13.6}$	
69	12:36:36.44	62:09:36.8	5.309	27.3	0.8 ± 0.1	$8.64^{+0.16}_{-0.40}$	$-2.20^{+0.12}_{-0.09}$	$0.75^{+0.17}_{-0.33}$	$5.6^{+6.3}_{-2.5}$	
67	12:36:40.27	62:09:36.7	5.313	–	2.6 ± 0.1	$9.09^{+0.54}_{-0.61}$	$-2.01^{+0.16}_{-0.08}$	$0.75^{+0.17}_{-0.49}$	$8.3^{+38.4}_{-4.1}$	
					Outside extended structures					
13227	12:36:58.22	62:14:18.7	5.151	27.7	1.2 ± 0.2	$8.51^{+0.25}_{-0.30}$	$-1.92^{+0.16}_{-0.15}$	$0.73^{+0.16}_{-0.28}$	$4.7^{+4.9}_{-2.5}$	
23280	12:37:22.17	62:16:14.0	5.165	26.9	4.1 ± 0.3	$8.51^{+0.31}_{-0.41}$	$-1.57^{+0.20}_{-0.27}$	$0.60^{+0.18}_{-0.14}$	$4.9^{+3.6}_{-2.5}$	
10911	12:36:24.08	62:13:51.2	5.197	26.3	3.6 ± 0.3	$9.40^{+0.12}_{-0.29}$	$-1.96^{+0.07}_{-0.04}$	$0.64^{+0.09}_{-0.27}$	$14.1^{+13.5}_{-5.6}$	[1]
74	12:36:40.52	62:09:37.9	5.207	–	2.1 ± 0.2	$8.41^{+0.44}_{-0.49}$	$-2.04^{+0.17}_{-0.15}$	$0.82^{+0.09}_{-0.11}$	$2.5^{+2.7}_{-1.2}$	
23026	12:36:19.92	62:16:10.9	5.208	27.6	2.1 ± 0.2	$8.61^{+0.21}_{-0.38}$	$-2.02^{+0.15}_{-0.11}$	$0.66^{+0.16}_{-0.33}$	$4.6^{+7.6}_{-2.5}$	
10200	12:36:22.49	62:13:42.3	5.216	27.6	6.9 ± 0.2	$7.92^{+0.22}_{-0.19}$	$-2.18^{+0.13}_{-0.14}$	$0.75^{+0.10}_{-0.07}$	$1.6^{+0.8}_{-0.8}$	
28662	12:37:06.58	62:17:53.2	5.216	27.4	1.3 ± 0.2	$8.58^{+0.19}_{-0.49}$	$-2.15^{+0.13}_{-0.10}$	$0.76^{+0.15}_{-0.23}$	$3.8^{+4.0}_{-2.1}$	
2930	12:36:22.49	62:11:39.5	5.222	23.5	5.0 ± 0.2	$11.07^{+0.13}_{-0.20}$	$-0.84^{+0.12}_{-0.16}$	$0.45^{+0.34}_{-0.15}$	$224.2^{+497.3}_{-187.2}$	
514	12:36:43.77	62:10:18.0	5.223	27.5	2.2 ± 0.2	$8.55^{+0.34}_{-0.32}$	$-1.96^{+0.16}_{-0.16}$	$0.74^{+0.17}_{-0.20}$	$3.7^{+3.2}_{-1.9}$	
11969	12:36:27.57	62:14:05.5	5.227	26.6	2.2 ± 0.3	$8.07^{+0.57}_{-0.24}$	$-2.22^{+0.08}_{-0.09}$	$0.91^{+0.05}_{-0.07}$	$2.5^{+4.0}_{-1.1}$	
21117	12:37:22.14	62:15:46.2	5.238	25.3	5.8 ± 0.5	$9.84^{+0.18}_{-0.26}$	$-1.73^{+0.14}_{-0.08}$	$0.64^{+0.15}_{-0.32}$	$61.2^{+113.4}_{-44.9}$	
21282	12:37:22.63	62:15:48.1	5.240	26.9	12.0 ± 0.3	$10.82^{+0.11}_{-0.31}$	$-1.49^{+0.09}_{-0.04}$	$0.01^{+0.01}_{0.00}$	$841.2^{+528.9}_{-322.7}$	
7135	12:36:19.66	62:12:56.8	5.246	27.5	9.9 ± 0.3	$7.57^{+0.15}_{-0.11}$	$-1.99^{+0.12}_{-0.13}$	$0.78^{+0.08}_{-0.08}$	$0.7^{+0.3}_{-0.1}$	
21068	12:36:11.21	62:15:45.8	5.247	28.1	1.4 ± 0.1	$8.41^{+0.31}_{-0.53}$	$-2.06^{+0.12}_{-0.11}$	$0.73^{+0.13}_{-0.14}$	$2.5^{+2.4}_{-1.5}$	
12053	12:36:22.48	62:14:05.3	5.248	27.4	2.2 ± 0.2	$8.37^{+0.38}_{-0.32}$	$-1.88^{+0.11}_{-0.12}$	$0.61^{+0.18}_{-0.15}$	$3.9^{+3.3}_{-2.0}$	
13670	12:37:27.33	62:14:23.6	5.250	26.8	2.0 ± 0.2	$8.37^{+0.40}_{-0.30}$	$-2.28^{+0.08}_{-0.07}$	$0.93^{+0.04}_{-0.14}$	$4.4^{+4.5}_{-2.2}$	
20423	12:37:07.73	62:15:37.4	5.272	25.7	6.5 ± 0.6	$9.56^{+0.29}_{-0.44}$	$-1.22^{+0.09}_{-0.11}$	$0.69^{+0.12}_{-0.23}$	$38.1^{+28.3}_{-22.6}$	

Notes. [a]1 = Walter et al. (2012), 2 = Arrabal Haro et al. (2018), 3 = Riechers et al. (2020), 4 = Calvi et al. (2021), 5 = Matthee et al. (2024), and 6 = Xiao et al. (2024).
[c]Presented in Xiao et al. (2024).

Table B5. Catalogues of star-forming galaxies at $z \sim 5.15-5.32$ that are part of the overdensity in the FRESCO GOODS North field.

ID	RA	Dec.	$z_{\rm spec}$	m_{210} [mag]	$f_{\rm H\alpha}$ [10^{-18}erg s^{-1} cm^{-2}]	log (M$_\star$)	β	A_V	SFR	Ref[a]
Outside extended structures										
17577	12:37:08.47	62:15:05.0	5.277	26.8	4.5 ± 0.2	$8.39^{+0.34}_{-0.38}$	$-2.28^{+0.08}_{-0.07}$	$0.89^{+0.05}_{-0.04}$	$3.2^{+2.4}_{-1.4}$	
1253	12:36:33.70	62:10:53.7	5.278	25.7	13.0 ± 0.4	$8.95^{+0.34}_{-0.34}$	$-2.18^{+0.10}_{-0.08}$	$0.72^{+0.14}_{-0.10}$	$10.8^{+8.8}_{-7.6}$	
983	12:36:46.13	62:10:44.8	5.280	29.0	1.9 ± 0.2	$6.90^{+0.16}_{-0.10}$	$-2.43^{+0.08}_{-0.05}$	$0.96^{+0.03}_{-0.04}$	$0.1^{+0.1}_{-0.0}$	
29634	12:36:39.58	62:18:23.1	5.288	27.3	1.8 ± 0.2	$8.22^{+0.19}_{-0.22}$	$-1.94^{+0.09}_{-0.10}$	$0.81^{+0.06}_{-0.09}$	$3.4^{+1.4}_{-1.1}$	
7294	12:37:13.04	62:12:59.5	5.292	27.9	10.0 ± 0.2	$7.72^{+0.26}_{-0.21}$	$-1.48^{+0.12}_{-0.12}$	$0.60^{+0.15}_{-0.13}$	$1.0^{+0.8}_{-0.3}$	
2243	12:36:52.12	62:11:22.7	5.296	28.0	2.4 ± 0.3	$8.18^{+0.43}_{-0.30}$	$-2.29^{+0.10}_{-0.15}$	$0.93^{+0.05}_{-0.13}$	$2.0^{+1.6}_{-0.6}$	
15255	12:36:03.80	62:14:39.7	5.315	26.0	3.8 ± 0.3	$9.15^{+0.37}_{-0.28}$	$-2.19^{+0.07}_{-0.10}$	$0.87^{+0.10}_{-0.21}$	$13.2^{+27.5}_{-6.7}$	
24012	12:36:29.52	62:16:25.0	5.316	27.6	1.5 ± 0.2	$8.33^{+0.32}_{-0.53}$	$-1.92^{+0.14}_{-0.14}$	$0.76^{+0.12}_{-0.19}$	$1.7^{+1.9}_{-0.8}$	

Notes. [a]1 = Walter et al. (2012), 2 = Arrabal Haro et al. (2018), 3 = Riechers et al. (2020), 4 = Calvi et al. (2021), 5 = Matthee et al. (2024), and 6 = Xiao et al. (2024).

[1]*Leiden Observatory, Leiden University, P.O. Box 9513, NL-2300 RA Leiden, the Netherlands*
[2]*Cosmic Dawn Center (DAWN), Niels Bohr Institute, University of Copenhagen, Jagtvej 128, København N, DK-2200, Denmark*
[3]*Department of Astronomy, University of Geneva, Chemin Pegasi 51, CH-1290 Versoix, Switzerland*
[4]*MIT Kavli Institute for Astrophysics and Space Research, 77 Massachusetts Ave., Cambridge, MA 02139, USA*
[5]*INAF – Osservatorio di Astrofisica e Scienza dello Spazio di Bologna, Via Gobetti 93/3, I-40129 Bologna, Italy*
[6]*Department for Astrophysical and Planetary Science, University of Colorado, Boulder, CO 80309, USA*
[7]*Departament d'Astronomia i Astrofísica, Universitat de València, C. Dr Moliner 50, E-46100 Burjassot, València, Spain*
[8]*Unidad Asociada CSIC 'Grupo de Astrofísica Extragaláctica y Cosmología' (Instituto de Física de Cantabria – Universitat de València)*
[9]*Max-Planck-Institut für Astronomie, Königstuhl 17, D-69117 Heidelberg, Germany*
[10]*Department of Physics, ETH Zürich, Wolfgang-Pauli-Strasse 27, CH-8093 Zürich, Switzerland*
[11]*Department of Physics, University of Bath, Claverton Down, Bath BA2 7AY, UK*
[12]*Department of Physics and Astronomy, University of California, Riverside, 900 University Avenue, Riverside, CA 92521, USA*
[13]*NSF's National Optical-Infrared Astronomy Research Laboratory, 950 N. Cherry Avenue, Tucson, AZ 85719, USA*
[14]*Instituto Astrofísica de Canarias (IAC), E-38205 La Laguna, Tenerife, Spain*
[15]*Departmento de Astrofísica, Universidad de La Laguna, E-38206 La Laguna, Tenerife, Spain*
[16]*Department of Physics & Astronomy, University of California, Los Angeles, 430 Portola Plaza, Los Angeles, CA 90095, USA*
[17]*Department of Astronomy, The University of Texas at Austin, 2515 Speedway, Stop C1400, Austin, TX 78712-1205, USA*
[18]*Astronomy Department, Yale University, 52 Hillhouse Ave, New Haven, CT 06511, USA*
[19]*Centre for Astrophysics and Supercomputing, Swinburne University of Technology, Melbourne, VIC 3122, Australia*
[20]*Department of Astronomy and Astrophysics, University of California, Santa Cruz, CA 95064, USA*
[21]*Centro de Astrobiología (CAB), CSIC-INTA, Ctra. de Ajalvir km 4, Torrejón de Ardoz, E-28850 Madrid, Spain*

This paper has been typeset from a TEX/LATEX file prepared by the author.